

1 **Future permafrost degradation under climate change in a headwater catchment of Central**  
2 **Siberia: quantitative assessment with a mechanistic modelling approach**

3 Thibault Xavier<sup>1</sup>, Laurent Orgogozo<sup>1\*</sup>, Anatoly S. Prokushkin<sup>2</sup>, Esteban Alonso-González<sup>3</sup>, Simon  
4 Gascoin<sup>4</sup>, Oleg S. Pokrovsky<sup>1,5</sup>

5 <sup>1</sup>Geoscience Environnement Toulouse (GET), CNRS, UMR5563, Toulouse, 31400, France

6 <sup>2</sup>V.N. Sukachev Institute of Forest SB RAS, Russia

7 <sup>3</sup>Instituto Pirenaico de Ecología, Consejo Superior de Investigaciones Científicas (IPE-CSIC), Jaca,  
8 Spain

9 <sup>4</sup>Centre d'Etudes Spatiales de la Biosphère, Université de Toulouse, CNRS/CNES/IRD/INRA/UPS,  
10 Toulouse, France

11 <sup>5</sup>BIO-GEO-CLIM Laboratory, Tomsk State University, Tomsk, Russia

12 \* *Corresponding author*: Laurent Orgogozo (laurent.orgogozo@get.omp.eu)

13 **Abstract**

14 Permafrost thawing as a result of climate change has major consequences locally and globally for  
15 the biosphere as well as for human activities. The quantification of its extent and dynamics under  
16 different climate scenarios is needed to design local adaptation and mitigation measures and to bet-  
17 ter understand permafrost climate feedbacks. To this end, numerical simulation can be used to ex-  
18 plore the response of soil thermal and hydrological regimes to changes in climatic conditions.  
19 Mechanistic approaches minimise modelling assumptions by relying on the numerical resolution of  
20 continuum mechanics equations, but they involve significant computational effort. In this work, the  
21 permaFoam solver is used along with high-performance computing resources to assess the impact  
22 of four climate scenarios of the Coupled Model Intercomparison Project Phase 6 (CMIP6) on per-  
23 mafrost dynamics within a pristine, forest-dominated watershed in the continuous permafrost zone.  
24 Using these century time-scale simulations, changes in the soil temperature, soil moisture, active  
25 layer thickness and water fluxes are quantified, assuming no change in the vegetation cover. The  
26 most severe scenario (SSP5-8.5) suggests a dramatic increase in both the active layer thickness and  
27 annual evapotranspiration, with the maximum values on the watershed in 2100 increasing by +65%  
28 and +35% compared to current conditions, respectively. For the active layer thickness, a variable  
29 that integrates both the thermal and hydrological states of the near-surface permafrost, this projected  
30 increase would correspond to a ~350 km southward shift in current climatic conditions. Moreover,  
31 in this scenario, the thermal equilibrium of near-surface permafrost with the new climatic conditions  
32 would not be reached in 2100, suggesting a further thawing of permafrost even in the case in which  
33 the climate change is halted.

## 34 **Keywords**

35 Permafrost, climate change, boreal forest, numerical modelling, high performance computing, soil  
36 temperature, soil moisture, evapotranspiration.

37

## 38 **1 Introduction**

39

40 Permafrost is mostly situated in regions that are experiencing especially intense climate  
41 change, resulting in widespread warming and thawing, with the shrinking of its lateral extent and  
42 the thickening of the soil active layer (Biskaborn et al., 2019; Hu et al., 2022; Li et al.; 2022a, b).  
43 Permafrost thawing induces sizable changes in the environment (Walvoord and Kurylyk, 2016;  
44 Nitze et al., 2018; Makarieva et al., 2019; Jin et al., 2022; Wright et al., 2022) and for human activi-  
45 ties (Shiklomanov et al., 2017; Strelestkiy et al., 2019, 2023; Hjort et al., 2018, 2022) in the Arctic  
46 and the sub-Arctic. For instance, a permafrost-thaw-related decrease in the soil moisture leads to an  
47 increase in boreal fire frequency (Kurylyk, 2019; Kim et al., 2020), while soil mechanical instabili-  
48 ties induced by permafrost thawing threaten human settlements (Ramage et al., 2021) and infra-  
49 structure (Bartsch et al., 2021). Moreover, permafrost thaw may exert significant controls on the  
50 biogeochemical cycles of carbon and related metals (Sonke et al., 2018; Karlsson et al., 2021;  
51 Walvoord and Striegl, 2021) and climate dynamics (Miner et al., 2022; Park and Kug, 2022; de  
52 Vrese et al., 2023), with potentially major feedback on climate warming. Thus, anticipating the evo-  
53 lution of permafrost cover and dynamics is of primary importance for understanding and mitigating  
54 the climate-change-induced impacts at high latitudes. For this, robust and accurate numerical simu-  
55 lations are required (Schneider von Deimling et al., 2022; Hu et al., 2023).

56 Boreal forest is one of the largest biomes on Earth (Gauthier et al., 2015), and 80% of its  
57 area is located in permafrost regions, and thereby covers 55% of the total global permafrost area  
58 (Stuenzi et al., 2021). Due to the complexity of the biophysical processes involved, quantifying the  
59 evolution of permafrost dynamics in boreal forests under climate change requires mechanistic, high-  
60 resolution modelling approaches (Orgogozo et al., 2019). However, the large extent of the consid-  
61 ered areas makes the use of such approaches impracticable at global, continental or regional scales.  
62 As a consequence, the mechanistic modelling of permafrost dynamics has to focus on processes at  
63 the watershed scale in headwater catchments with long-term environmental monitoring, following a  
64 general trend in the Arctic sciences (Speetjens et al., 2023; Vonk et al., 2023). In Arctic environ-

65 ments, the vegetation strongly controls the surface energy budget (Fedorov et al., 2019; Oehri et al.,  
66 2022), interacts with climate dynamics (Park et al., 2020; Kirilyanov et al., 2024) and drives water  
67 fluxes (Orgogozo et al., 2019). As such, vegetation should be taken into account when simulating  
68 the impact of climate warming on permafrost in boreal forest areas (Lorantý et al., 2018, Kirilyanov  
69 et al., 2020; Holloway et al., 2020).

70 The quantitative mechanistic modeling of permafrost dynamics under climate change at the head-  
71 water catchment scale requires large computational resources, because fine spatio-temporal dis-  
72 cretization is needed due to the strong non-linearities and couplings of various physical processes  
73 (Kurylyk and Watanabe, 2013). This is especially important for century long simulation periods  
74 (O'Neill et al., 2016) and simulation domains with surfaces of up to tens of square kilometres (e.g.  
75 Arndal and Torp-Jørgensen, 2020). For this, high performance computing techniques are needed  
76 (Orgogozo et al., 2023).

77 In this study, we focus on a permafrost-dominated, forested watershed of central Siberia that  
78 was subjected to long-term environmental monitoring, the Kulingdakan watershed (e.g. Prokushkin  
79 et al., 2007; Mashukov et al., 2021). The objective is to assess the future state of the permafrost and  
80 the ground thermal regime in this continuous-permafrost, boreal forest environment under different  
81 climate change scenarios at the century time scale. The permafrost status of this catchment under  
82 current climatic conditions has already been investigated (Orgogozo et al., 2019). Here, we simu-  
83 late, using a mechanistic modelling approach, the permafrost dynamics at the catchment scale until  
84 2100 under various scenarios of climate change. The vegetation controls on permafrost dynamics  
85 are partly included in the mechanistic modelling framework, considering evapotranspiration fluxes  
86 (Orgogozo et al., 2019), and partly handled empirically, via accounting for the insulating effect of  
87 ground-floor vegetation (Blok et al., 2011; Cazaurang et al., 2023). However, because no changes in  
88 vegetation are explicitly considered, we assume constant biomass and primary production and  
89 therefore investigate only the physical part of the response of permafrost to climate change. We use  
90 the permaFoam high performance computing cryohydrogeological simulator (Orgogozo et al.,  
91 2023) with a national-level supercomputing infrastructure, the Joliot-Curie supercomputer of the  
92 Très Grand Centre de Calcul (TGCC) of the French Alternative Energies and Atomic Energy Com-  
93 mission (CEA). The simulated permafrost thawing features in Kulingdakan are discussed and com-  
94 pared for different CMIP6 (Coupled Model Intercomparison Project Phase 6) scenarios, including  
95 the following:

- 96 - the soil thermal regime (soil temperature and active layer thickness evolution, equivalent south-
- 97 ward shift under current climatic conditions);
- 98 - the soil hydrology (evapotranspiration fluxes and soil moisture evolution);
- 99 - the spatial variability of climate warming impacts at the scale of the watershed under study;
- 100 - the state and evolution of the thermal imbalance of the permafrost (e.g. Ji et al., 2022; Nitzbon et
- 101 al., 2023) in the considered region.

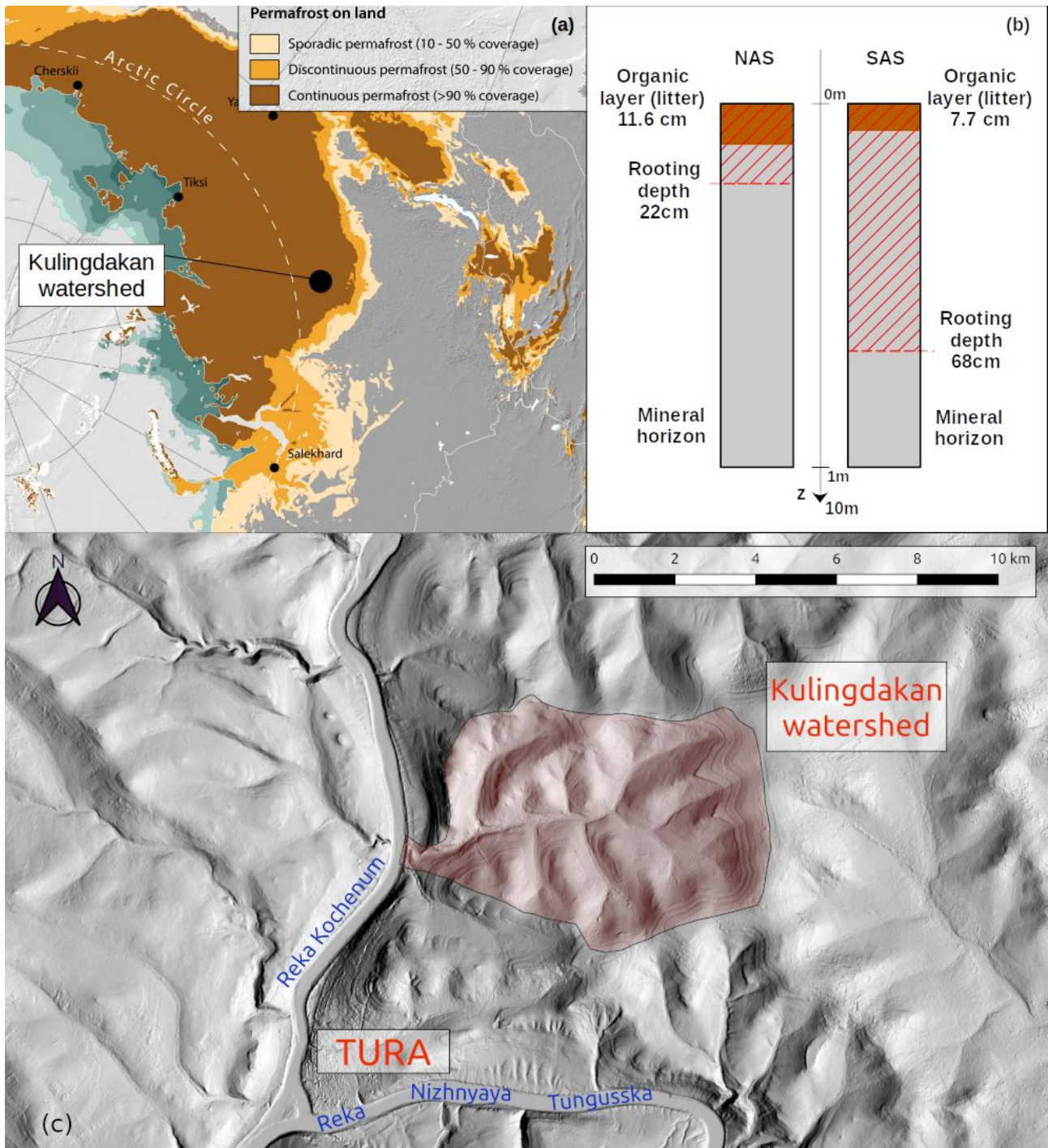
## 102 **2 Materials and methods**

### 103 **2.1 Study site: Kulingdakan, a forested catchment in continuous-permafrost area**

104 The Kulingdakan catchment is located in the Krasnoïarsk region (64.31°N, 100.28°E),  
105 within a continuous permafrost zone, belonging to the boreal forest biome (Northern Taïga – see  
106 Fig. 1a). This pristine catchment has been monitored for the study of boreal processes over the past  
107 two decades. The vegetation is dominated by larch (*Larix gmelinii*), dwarf shrubs, mosses and  
108 lichens. The catchment covers an area of 41 km<sup>2</sup> and has an elevation ranging from 132 m to 630 m  
109 (Prokushkin et al., 2004). The climate is cold and continental, with an average annual mean temper-  
110 ature of -8°C and an annual total precipitation of 400 mm (annual mean measured between 1999  
111 and 2014 at the Tura meteorological station, 5 km south of the Kulingdakan catchment, altitude of  
112 168 m). The stream, which flows from east to west, divides the 41 km<sup>2</sup> catchment area into two ap-  
113 proximately rectangular slopes of equal area, the North Aspect Slope (NAS) and the South Aspect  
114 Slope (SAS). As shown by a previous numerical study using permaFoam of this site under current  
115 climatic conditions, the hydrological budget in this watershed is largely dominated by evapotranspi-  
116 ration fluxes (Orgogozo et al., 2019). Two horizons constitute the soil in the first few metres: an or-  
117 ganic horizon (litter and peat) and a mineral horizon (mainly rocky/gravelly loam).

118 Due to the difference in solar radiation induced by their aspects, primary production and  
119 evapotranspiration are more intensive in the SAS than in the NAS. Thus the two slopes show signif-  
120 icant differences in the larch tree size and larch stand density, as well as in the rooting depth, or-  
121 ganic horizon and moss layer thickness and active layer dynamics. The thickness of the organic  
122 horizon is 11.6 cm on the NAS and 7.7 cm on the SAS (Gentsch, 2011), while the moss layer thick-  
123 ness is 13 cm on the NAS and 6.4 cm on the SAS (Prokushkin et al., 2007). The rooting depth is 10  
124 cm into the mineral horizon for the NAS and 60 cm for the SAS (Viers et al., 2013), and this differ-  
125 ence has been shown to be of great importance for the dynamics of the active layer (Orgogozo et al.,  
126 2019). The observed maximum active layer thickness is 1.22 m in the SAS and 0.58 m in the NAS

127 (Gentsch, 2011). These pedological and physiological contrasts between the two aspects of the wa-  
 128 tershed slope, summarised in Figure 1b, are explicitly considered when performing permafrost sim-  
 129 ulations (Supplementary Material B – [Calculation set-up and details](#)).  
 130



131 **Figure 1: (a) Location of Kulingdakan watershed (map from GRID-Arendal/Nunataryuk). (b)**  
 132 **Representation of soil column structure for North Aspected Slope (NAS) and South Aspected**

133 **Slope (SAS) of the Kulingdakan watershed. (c) Digital Elevation Model (DEM) of Kuling-**  
 134 **dakan watershed, extracted from ArcticDEM (Porter et al., 2023).**

135 Previous modelling studies in the Kulingdakan catchment on water flux repartition, the soil  
 136 temperature at different depths and the active layer thickness (Orgogozo et al., 2019; Orgogozo et  
 137 al., 2023) demonstrated that the use of the permaFoam solver, together with boundary conditions  
 138 (water fluxes and soil surface temperature) provided by field measurements, made it possible to ob-  
 139 tain numerical simulation results in agreement with in-situ observations under current climatic con-  
 140 ditions .

## 141 **2.2 The permaFoam cryohydrogeological simulator**

142 The numerical tool used in this study is permaFoam (Orgogozo et al., 2019, 2023), the per-  
 143 mafrost modelling solver developed in the framework of OpenFOAM, the open source, high perfor-  
 144 mance computing tool box for computational fluid dynamics (Weller et al., 1998, openfoam.org,  
 145 openfoam.com). This solver is designed to simulate 3D, transient coupled heat and water transfers  
 146 in a variably saturated soil with evapotranspiration and the freezing/thawing of the pore water. The  
 147 two main equations solved by permaFoam are the Richards equation (Eq. (1)), which governs the  
 148 flow of water, and an energy balance equation (Eq. (2)) that governs the heat transfer; both are de-  
 149 fined at the Darcy scale of the considered porous medium (soil):

150

$$C_H(h) \frac{\partial h}{\partial t} = \nabla \cdot (K_H(h, T) \cdot \nabla (h+z)) + Q_{AET}(h, t) \quad (1)$$

$$\frac{\partial \left( \left( C_{T,eq}(h, T) + L \frac{\partial \theta_{ice}(h, T)}{\partial T} \right) T \right)}{\partial t} + \nabla \cdot (V(h, T) C_{T,liquid} T) = \nabla \cdot (K_{T,eq}(h, T) \nabla T) \quad (2)$$

151

152 The two primary variables in Eqs, (1) and (2) are the generalised water pressure head  $h$  [m] and the  
 153 soil temperature  $T$  [K], respectively. In the Richards equation (Eq. (1)),  $z$  is the vertical coordinate  
 154 [m] (oriented upward),  $K_H$  is the hydraulic conductivity of the variably saturated, variably frozen  
 155 porous medium [ $\text{m}\cdot\text{s}^{-1}$ ],  $C_H$  is the capillary capacity (also called the specific moisture capacity) of  
 156 the unsaturated porous medium [ $\text{m}^{-1}$ ] and  $Q_{AET}$  [ $\text{s}^{-1}$ ] is a source term representing the water uptake  
 157 by vegetation through the evapotranspiration process (computed using the Hamon formula; see Ha-  
 158 mon, 1963; Frolking, 1997). From the pressure head field  $h$ , the Darcy velocity  $V$  [ $\text{m}\cdot\text{s}^{-1}$ ] is derived  
 159 according to Eq. (3):

$$V(h, T) = K_H(h, T) \cdot \nabla(h + z) \quad (3)$$

160

161 In the energy balance equation (Eq. (2)), the considered transfer processes are conduction through  
 162 the entire porous medium, convection by pore water flow, and latent heat exchanges when phase  
 163 change occurs. In this heat transfer equation,  $K_{T,eq}$  [ $J \cdot m^{-1} \cdot s^{-1} \cdot K^{-1}$ ] is the apparent thermal conductivity  
 164 of the porous medium,  $\theta_{ice}$  [-] is the volumetric ice content,  $L$  [ $J \cdot m^{-3}$ ] is the latent heat of fusion of  
 165 ice,  $C_{T,eq}$  [ $J \cdot m^{-3} \cdot K^{-1}$ ] is the equivalent heat capacity of the porous medium, and  $C_{T,liquid}$  [ $J \cdot m^{-3} \cdot K^{-1}$ ] is the  
 166 equivalent heat capacity of liquid water. In permaFoam these two coupled equations are solved in  
 167 3D using the finite volumes method, with sequential operator splitting for handling the couplings,  
 168 Picard loops for dealing with the non-linearities and a backward time scheme for temporal discreti-  
 169 sation. A detailed description of the solver can be found in Orgogozo et al. (2023).

170 The numerical resolution of these coupled and highly non-linear equations, including stiff  
 171 fronts generated by freeze/thaw processes, at the space and time scales required for studying climate  
 172 change impacts on boreal watersheds requires both a robust algorithm and the efficient use of high  
 173 performance computing means. This is the reason that permaFoam is developed within the Open-  
 174 FOAM framework, which allows the use of up-to-date and efficient numerical methods for solving  
 175 partial differential equations on last-generation supercomputing facilities. Thanks to its implementa-  
 176 tion in OpenFOAM, the permaFoam solver has demonstrated excellent parallel performances on  
 177 various supercomputer architectures for dedicated test cases (Orgogozo et al., 2023), both in terms  
 178 of large numerical domains (up to 1 billion mesh points on the CALMIP Olympe supercomputer)  
 179 and the number of cores (16,000 on the GENCI IRENE-ROME supercomputer).

180

### 181 **2.3 Modelling domain**

182 According to preliminary numerical experiments (data not shown), for modelling Kuling-  
 183 dakan watershed permafrost the use of a dual 2D simplified representation (Orgogozo et al., 2019)  
 184 makes it possible to simulate properly the thermal and hydrological fluxes in the soils. As such, full  
 185 3D simulations, which are far more costly from a computational perspective than 2D simulations  
 186 (Orgogozo et al., 2023), are not needed. Additionally, the use of 2D simulations allows the consid-  
 187 eration of lateral transfers (Sjöberg et al., 2016; Lamontagne-Hallé et al.; 2018, Hamm and Framp-  
 188 ton, 2021; Jan, 2022). Thus, in this work we used 2D numerical domains, with climatic forcing as  
 189 the top boundary conditions (see section 2.4) and geothermal heat flux and nil water flux as the bot-

190 tom boundary conditions. The initial conditions were obtained by 10 years of spin-up under current  
191 climatic conditions. These current climatic conditions were represented by a synthetic year of cli-  
192 mate forcing corresponding to the multi-annual means of the 1999–2014 observations (see Supple-  
193 mentary Material A- [Estimating soil surface temperature from external conditions](#), including Fig.  
194 S1). The starting conditions of this spin-up were extracted from the results of the previous calcula-  
195 tions (Orgogozo et al., 2019). The convergence criterion for the spin-up was the active layer thick-  
196 ness inter-annual difference (annual variability less than 0.2%). The spatial discretisation of the do-  
197 main is done using a mesh of  $5.2 \times 10^7$  cells, according to a convergence study presented in Supple-  
198 mentary Material B - [Calculation set up and details](#)).

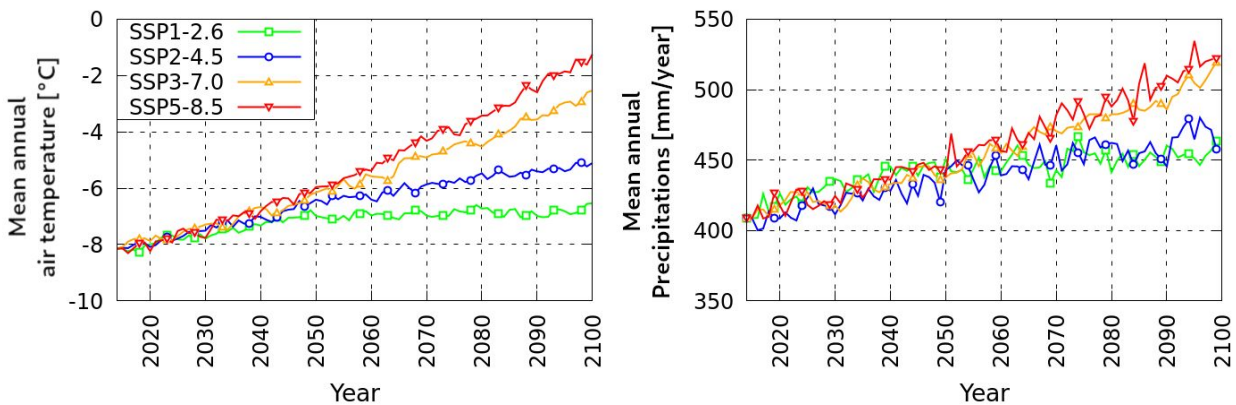
199 The numerical simulations provide the full 2D fields of physical quantities describing the  
200 heat and water flow within both the SAS and NAS (two 2.5-km-wide, 10-m-thick slopes), including  
201 both the frozen and active layers in each slope. These included the soil temperature, pressure head,  
202 liquid water content and ice content for each time step that was saved (user defined; here, every 6  
203 months). In addition, the temperature, water content, ice content and evapotranspiration sink term  
204 are monitored at an hourly frequency throughout two vertical profiles located at the mid-slope of  
205 the SAS and NAS numerical domains, using 61 virtual point probes distributed over the 10 m of the  
206 numerical domain thickness. Finally, the infiltration and exfiltration water fluxes through the total  
207 soil surface are also saved from the standard output at every time step. Further details of modelling  
208 set up are presented in Supplementary Material B – [Calculation set up and details](#)..

## 209 ***2.4 Soil surface conditions under climate change derived from CMIP6 scenarios***

210 In order to apply climate forcings that are representative of possible future trajectories, we  
211 consider climate scenarios produced as a part of the Coupled Model Intercomparison Project Phase  
212 6 (CMIP6) organised by the Intergovernmental Panel on Climate Change (IPCC) (Eyring et al.,  
213 2016); in particular, we consider the so-called tier-1 key scenarios (O’Neill et al., 2016). These sce-  
214 narios have been highlighted because of their relevance to scientific questions, the range of possible  
215 futures they cover, and their continuity with previous representative common pathways (RCP) sce-  
216 narios (van Vuuren et al., 2011) published during CMIP5. We considered four CMIP6 scenarios,  
217 from sustainable pathway with the least forcing (coldest) to the pathway with the most forcing  
218 (hottest): SSP1-2.6, SSP2-4.5, SSP3-7.0 and SSP5-8.5. Among these scenarios, SSP2-4.5 is the one  
219 most often used in permafrost studies (e.g. Karjalainen et al., 2019; Ramage et al., 2021; Hjort et  
220 al., 2022). For each of these scenarios, an ensemble of models has been run on different regions of



221 the globe. The climate model output data were accessed via the IPCC Working Group I (IPCC-  
 222 WGI) Interactive Atlas (Iturbide et al., 2021), February 2023 version, which provides the median  
 223 (P50) of the ensemble of models for a selected output variable, region and scenarios. We used the  
 224 projections of the air temperature and precipitation changes for the East Siberian region, averaged at  
 225 each yearly time step. To obtain the local scenarios of climate change for the air temperature and  
 226 precipitation (Fig. 2), these yearly averaged projections of air temperature / precipitation changes  
 227 between 2015 and 2100 have been summed with daily air temperature / precipitation variations  
 228 along the synthetic year of climate forcing corresponding to the multi-annual means of the 1999–  
 229 2014 observations in Tura, which are representative of current climatic conditions (see Supplemen-  
 230 tary Material A - **Estimating soil surface temperature from external conditions**, Fig. S1). This pro-  
 231 vided the projections of the daily air temperature / precipitation from 2015 to 2100 for the Tura  
 232 area. The yearly averages of these daily projections are presented in Figure 2.  
 233



234  
 235 **Figure 2: Projections of air temperature and precipitation in Kulingdakan based on CMIP6**  
 236 **projections on the Eastern Siberia area.**

237 The projections show an increase in the air temperature over the century, with a rate be-  
 238 tween  $+1.9^{\circ}\text{C}/100$  years (SSP1-2.6) and  $+7.8^{\circ}\text{C}/100$  years (SSP5-8.5); these rates were obtained by  
 239 re-scaling the averaged increase rates from 2014 to 2100 to the centennial time scale. For every sce-  
 240 nario this local increase rate is higher than the global one (global increase rates, according to Fan et  
 241 al. [2020]: SSP1-2.6:  $+1.18^{\circ}\text{C}/100$  ears; SSP2-4.5:  $+3.22^{\circ}\text{C}/100$  years; SSP3-7.0:  $+5.50^{\circ}\text{C}/100$   
 242 years; SSP5-8.5:  $+7.20^{\circ}\text{C}/100$  years). The annual precipitation could also change significantly, with  
 243 a relative increase in 2100 of  $+12\%$  (SSP1-2.6) to  $+29\%$  (SSP5-8.5) compared to the current value.

244 In order to translate these climate projections, which describe atmospheric conditions, into  
 245 suitable soil surface boundary conditions for cryohydrogeological simulations (water fluxes and

246 temperature at the soil surface, beneath snow and moss layers), a dedicated empirical procedure has  
247 been developed. The goal is to set up a methodology for deriving the soil surface temperature from  
248 the air temperature on the slopes of the Kulingdakan watershed, based on the available observation  
249 data. Indeed, the soil temperature and air temperature may be significantly different in such a boreal  
250 forest environment, due to the effects of understorey (Zellweger et al., 2019; Haesen et al., 2021),  
251 moss cover insulation (Blok et al., 2011; Cazaurang et al., 2023), the winter snowpack (Jan and  
252 Painter, 2020; Khani et al., 2023) and its interactions with vegetation (Dominé et al., 2022). This  
253 empirical, site-specific procedure is detailed in Supplementary Material A - **Estimating soil surface**  
254 **temperature from external conditions**), and it makes it possible to build up slope-wise soil tempera-  
255 ture estimates on the basis of the air temperature and snow conditions. For water fluxes, the sim-  
256 plest approximation has been adopted, assuming that the water flux at the top of the soil is equal to  
257 the rain flux. For the soil surface temperature estimate, we first used a modified temperature index  
258 approach (Braithwaite and Olesen; 1989, Hock 2003) for estimating the snow water equivalent, and  
259 then we used multiple regression to derive below-moss soil surface temperature from the air tem-  
260 perature, precipitation and snow water equivalent. We chose a temperature index approach to simu-  
261 late the snow water equivalent on the soil surface because climate projections only provide the air  
262 temperature and precipitation, whereas a more advanced energy balance snowpack model requires  
263 additional information on wind, radiation, and air humidity. To calibrate this temperature index  
264 model we first reconstruct the snow water equivalent for the period 1999–2014 from the observed  
265 snow depth with the Multiple Snow Data Assimilation System (MuSA) toolbox (Alonso-González  
266 et al., 2022) forced with ERA5 data (Hersbach et al., 2020), fusing available snow depth observa-  
267 tions with an ensemble of simulations generated by the energy and mass balance model called the  
268 Flexible Snow Model (Essery, 2015). Then, we calibrated a multiple regression method to derive  
269 the soil surface temperature as a function of the air temperature and precipitation, while taking into  
270 account the insulating effect of moss and snow layers. Calibrations were performed with air temper-  
271 ature and precipitation data measurements, the MuSA-derived snow water equivalent between 1999  
272 and 2014 and the top-soil (i.e. below moss) temperature measured in situ between 2003 and 2005.  
273 With this procedure, for each slope, an empirical transfer function that provides soil temperature es-  
274 timates derived from the air temperature and precipitation was obtained. Finally, these transfer  
275 functions were used to produce scenarios of the daily soil surface temperature under climate change  
276 for the two slopes of the catchment. This information is to for build the soil surface boundary condi-  
277 tions of the hydrogeological simulations. It must be emphasised that our empirical approach was

278 based on parametrical fitting on observation data for estimating the transfer function between atmo-  
279 spheric forcing and the soil surface temperature. As a result, no vegetation changes due to climate  
280 change could be considered in this transfer function. Therefore, we focus on the purely physical re-  
281 sponse of the catchment permafrost to climate change, while considering the vegetation impacts on  
282 permafrost dynamics at constant vegetation cover. Coupling a vegetation dynamics with the cryohy-  
283 drogeological model would allow one to assess the impact of the climate warming-induced changes  
284 of the vegetation cover on permafrost conditions. However, this is beyond the scope of the present  
285 study and will be the focus of future work.

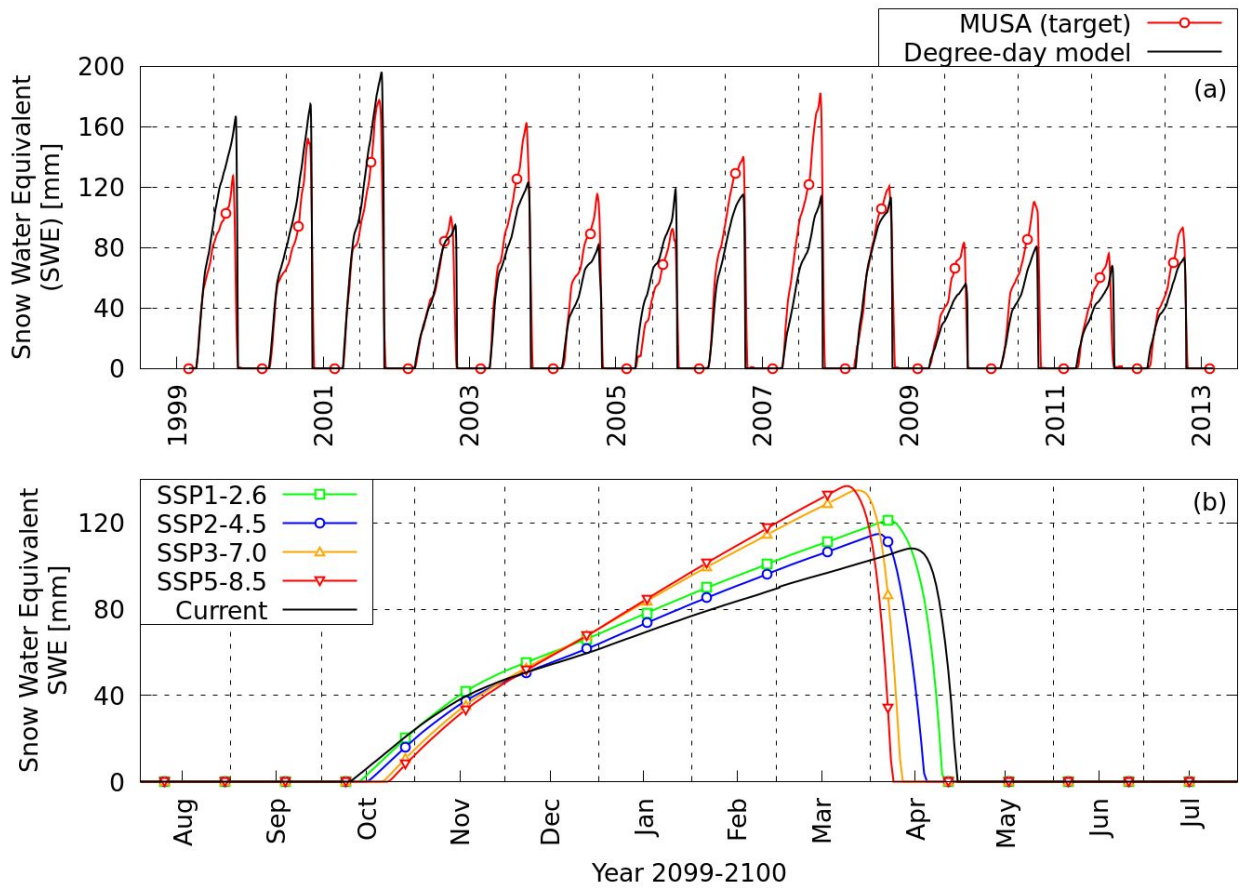
## 286 **3 Results**

287  
288 From post-processing the computed 2D fields of physical quantities describing the heat and water  
289 flow within both the SAS and NAS (two 2.5-km-wide, 10-m-thick slopes), including both frozen  
290 and active layers in each slope, a large wealth of data characterising the considered virtual per-  
291 mafrost dynamics is obtained (Supplementary Material C – **Changes in the main variables accord-**  
292 **ing to the four climate projections**), and below, only the key features of the centennial evolution un-  
293 der climate change are presented.

### 295 **3.1 Soil surface temperature projections**

296 The results of the temperature index approach used for modelling the snow cover of the Kuling-  
297 dakan watershed is presented in Figure 3. The snow water equivalent (SWE) model shows a good  
298 agreement with the MuSA reconstructions (Fig. 3a); hence, this model was used to estimate the  
299 SWE under future climate projections (Fig. 3b).

300

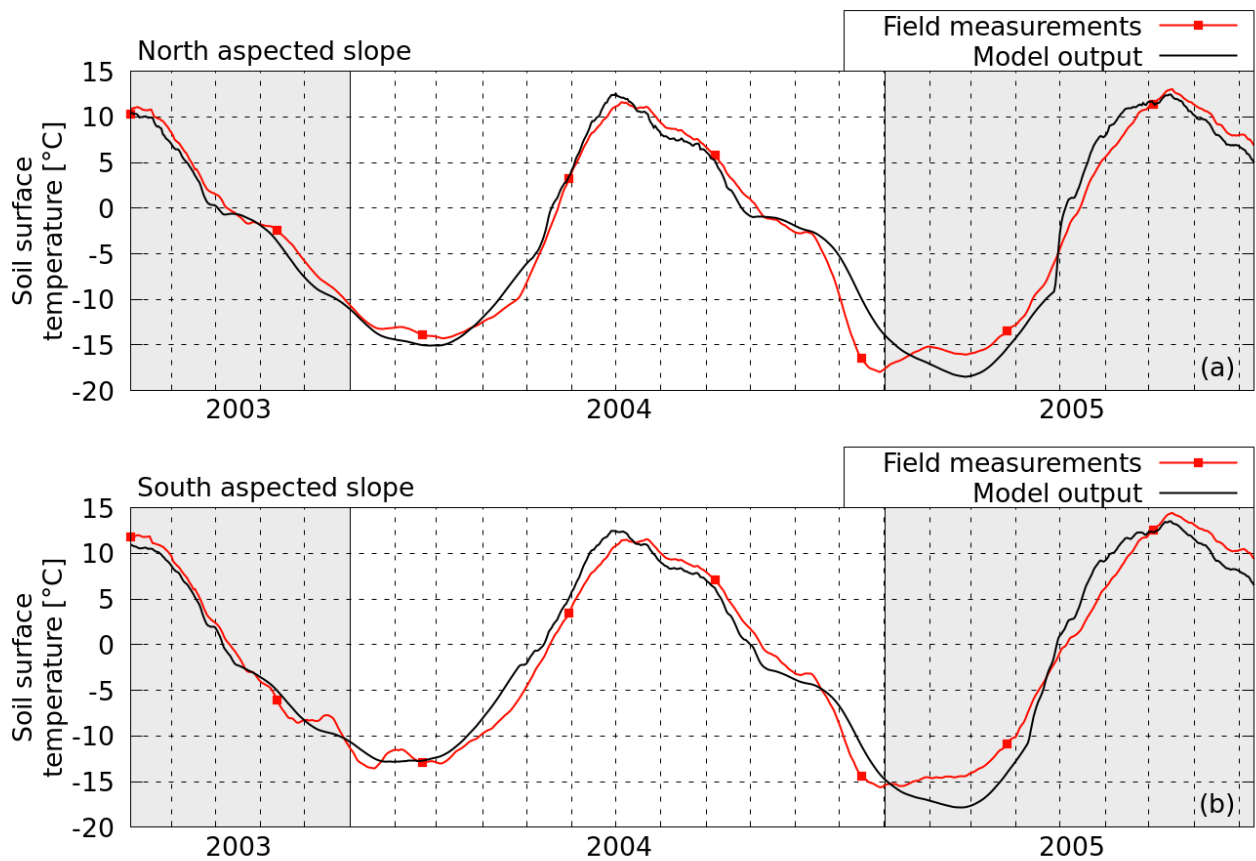


301

302 **Figure 3: (a) Present snow model comparison with MuSA output and (b) projection at the end**  
 303 **of the century.**

304 For each slope, the output data of the snow cover model were used as input data for the multiple re-  
 305 gression of the soil surface temperature, along with the air temperature data and precipitation data.  
 306 These empirical transfer functions were in good agreement with the observations, as shown in Fig-  
 307 ure 4.

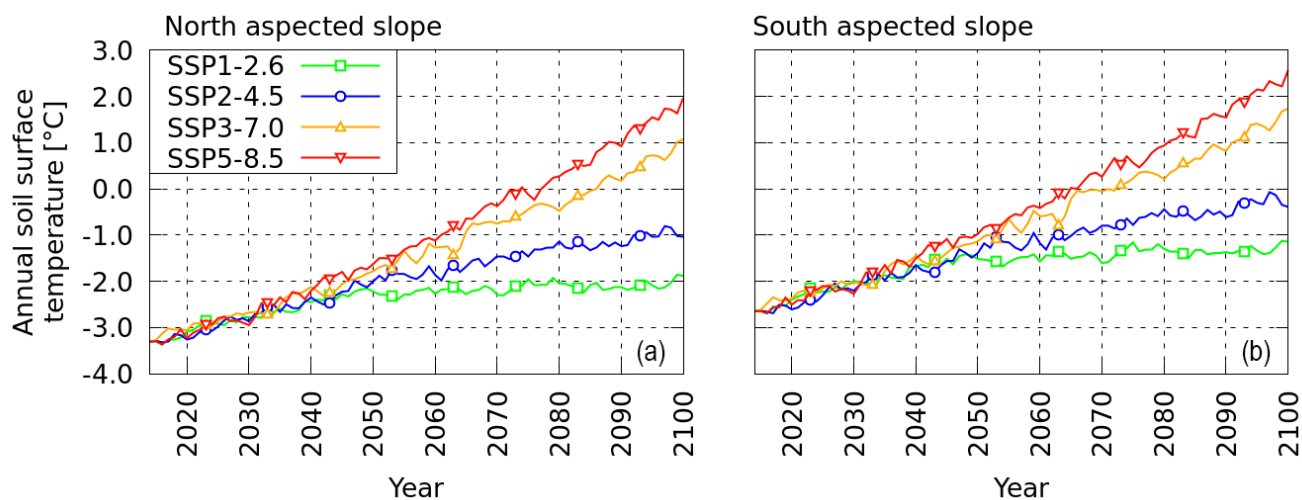
308



309

310 **Figure 4: Measurements and empirical transfer function estimates for soil surface tempera-**  
 311 **ture in present climatic conditions in (a) NAS and (b) SAS.**

312 The L1 norm of the differences between the field measurements and model output is 1.42°C in the  
 313 NAS, and 1.56°C in the SAS. The L2 norms of these differences are 0.07°C for both the SAS and  
 314 NAS. A more detailed discussion of the behaviour of these empirical transfer functions may be  
 315 found in Supplementary Material A – **Estimating soil surface temperature from external conditions.**  
 316 Finally, for each slope, soil temperature projections are obtained for the four considered CMIP6 cli-  
 317 mate scenarios by applying the developed modelling chain with the projections for air temperature  
 318 and precipitation as input data.



319

320 **Figure 5: Soil surface temperature projections over the century based on SSP scenarios ob-**  
 321 **tained using the transfer function described in Supplementary Material A – Estimating soil**  
 322 **surface temperature from external conditions.** Transfer function model estimation for soil  
 323 **surface temperature at present conditions for (a) the NAS and (b) SAS of the Kulingdakan**  
 324 **watershed(b).**

325

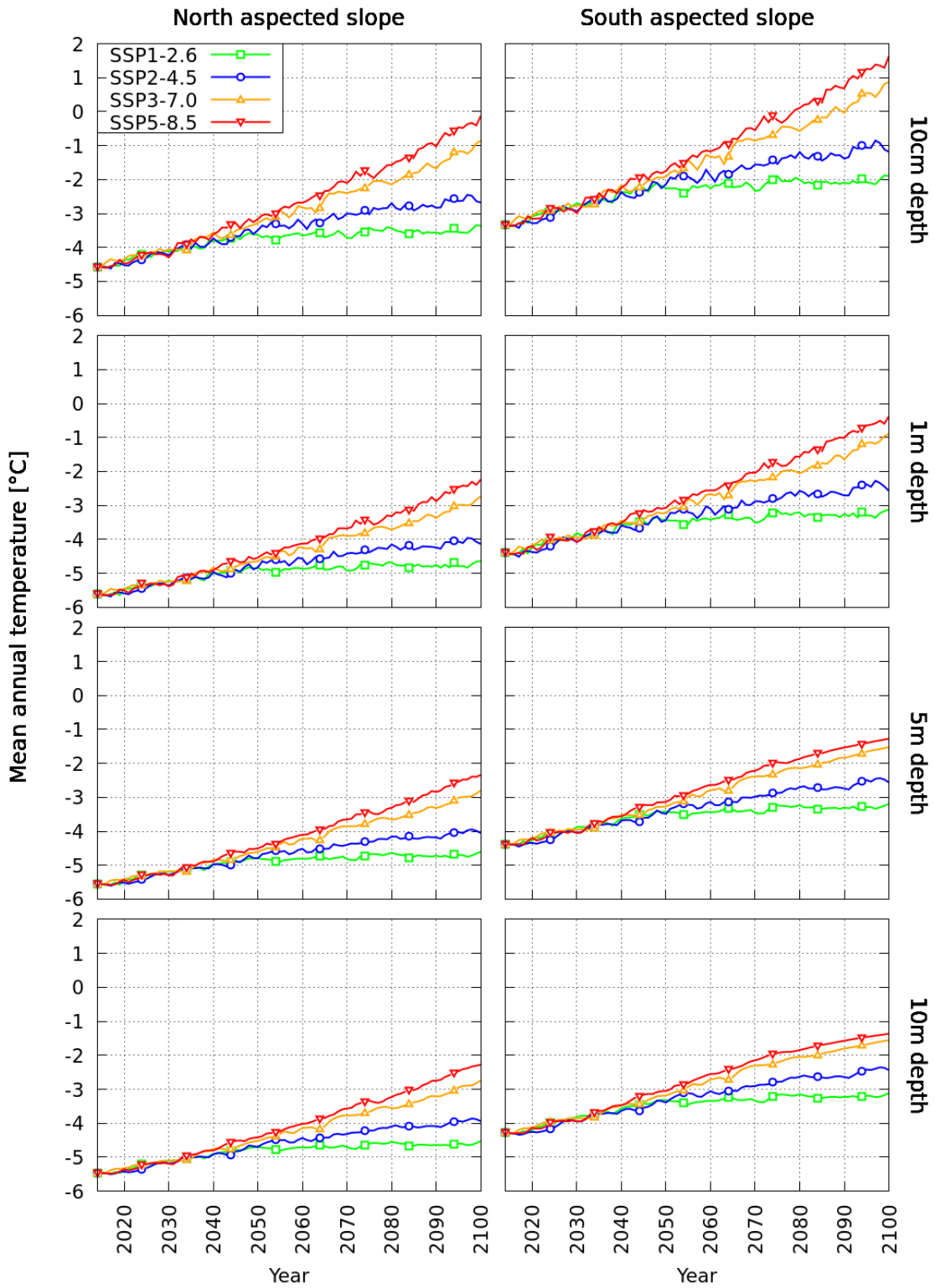
326 The four projections based on the different Shared Socioeconomics Pathways (SSPs) lead to an in-  
 327 crease in the ground surface temperature from +1.4°C (SSP1-2.6) to +5.2°C (SSP5-8.5) between  
 328 2014 and 2100 (Fig. 5a and 5b). These rates of increase, roughly equivalent by extrapolation to  
 329 +1.7°C/100 years (SSP1-2.6) and +5.9°C/100 years (SSP-8.5), are lower than the projected in-  
 330 creases in air temperature (+1.9°C/100 years for SSP1-2.6 and +7.8°C/100 years for SSP5-8.5) due  
 331 to the insulating effect of the snow cover and the vegetation layer, and also due to the thermal iner-  
 332 tia of the soil column below the surface. One can note that for the SSP3-7.0 and SSP5-8.5 scenarios,  
 333 the mean annual soil surface temperature becomes positive around 2080.

### 334 3.2 Trends in soil temperatures

335 The soil temperature at different depths is one of the key variables for characterising per-  
 336 mafrost dynamics. The multi-annual trends induced by the climate warming of the mean annual soil  
 337 temperature between 2014 and 2100 at four depths (10 cm, 1 m, 5 m and 10 m below the surface)  
 338 are illustrated in Figure 6.

339

340

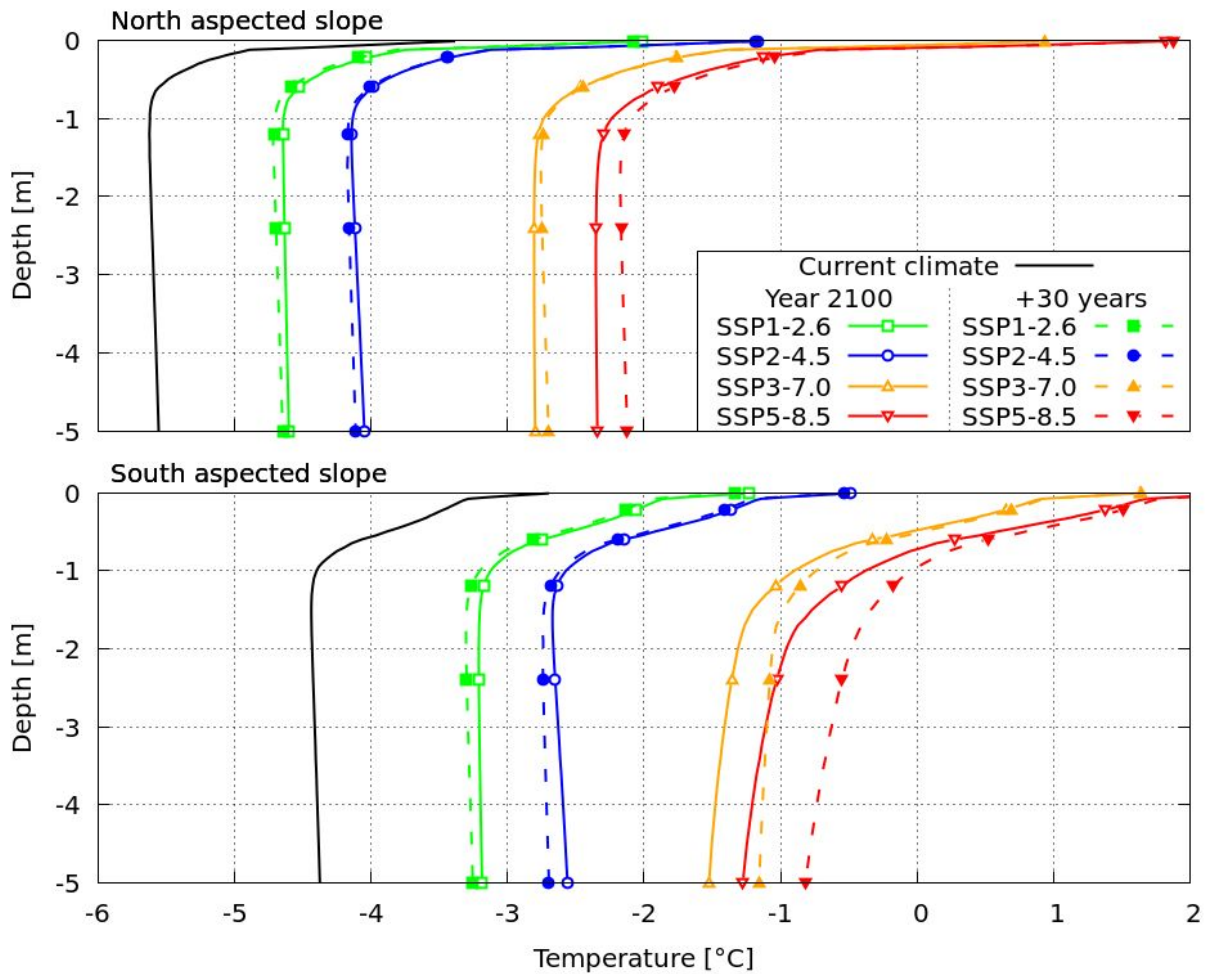


341

342 **Figure 6: Mean annual temperature evolution at 10 cm, 1 m, 5 m and 10 m under the surface**  
 343 **for each scenario and slope considered.**

344 On both slopes, the soil temperature experiences a significant increase down to 10 m depth,  
345 for all climate warming scenarios considered. The annual mean soil temperature even becomes pos-  
346 itive close to the surface (10 cm depth) in the SAS for the two high- forcing pathway (hottest) sce-  
347 narios, by 2080 for SSP5-8.5 and by 2090 for SSP3-7.0. Meanwhile, for the medium scenario  
348 SSP2-4.5 and for the low-forcing sustainable pathway (coldest) scenario SSP1-2.6, the mean annual  
349 soil temperature stays negative everywhere until 2100. The warming is more intensive in the SAS  
350 than in the NAS, and, as expected, the amplitude of soil warming decreases with depth. In the SAS,  
351 at 10 cm depth the temperature rise between current conditions and the year 2100 is 1.4 °C for the  
352 SSP1-2.6 scenario and 5.0 °C for the SSP5-8.5 scenario, while at 5 m depth, the temperature rises  
353 are 1.2°C and 3.1°C, respectively. In the NAS, at 10 cm depth the temperature rise between current  
354 conditions and the year 2100 is 1.2°C for the SSP1-2.6 scenario and 4.4°C for the SSP5-8.5 sce-  
355 nario, while at 5 m depth, the temperature rises are 1.0°C and 3.2°C, respectively. It should be noted  
356 that, for both slopes, the vertical gradient of the temperature in 2100 is higher in scenario SSP5-8.5  
357 than in scenario SSP1-2.6. This indicates a stronger thermal non-equilibrium under more intense  
358 warming. For instance, the difference in temperature in 2100 between 10 cm depth and 5 m depth is  
359 3.0°C in the SAS and 2.2 °C in the NAS for scenario SSP5-8.5, while it is 1.3°C in the SAS and  
360 1.2°C in the NAS for the SSP1-2.6 scenario. In order to provide insight into the thermal equilibrium  
361 state of the soil columns in each slope in 2100, additional simulations have been performed by ap-  
362 plying the projected climatic conditions of the end of the century (averaged over 2096–2100) for 30  
363 more years. For each scenario, the vertical soil temperature profiles for 2100 and for the numerical  
364 experiments with 30 more years of 2096–2100 climatic conditions are plotted in Figure 7.





365

366 **Figure 7: Annual mean temperature profiles in 2100 and after 30 years of additional cycling**  
 367 **of the average climatic forcing between 2096 and 2100.**

368

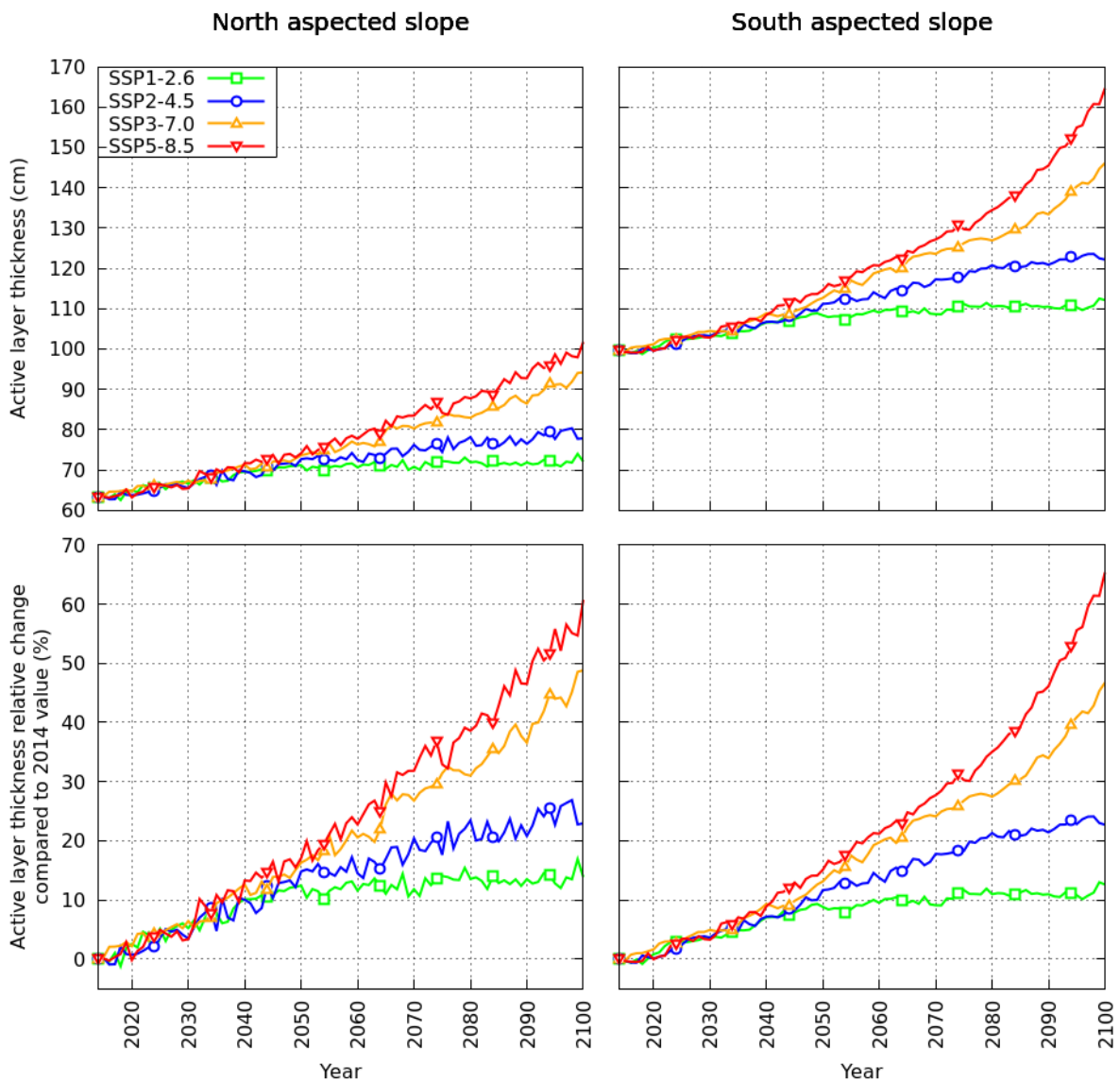
369 Considering the soil temperature profiles in 2100, two regions may be distinguished: the  
 370 first metre, with steep positive vertical gradients (the soil surface is warmer than the bottom of the  
 371 active layer), and a deeper region, with smoother vertical thermal gradients that are either slightly  
 372 negative (SSP1-2.6 and SSP2-4.5 in the NAS and SAS), almost nil (SSP3-7.0 and SSP5-8.5 in the  
 373 NAS) or positive (SSP3-7.0 and SSP5-8.5 in the SAS). When comparing these profiles with those  
 374 obtained with 30 additional years of modelling in constant ‘2096–2100’ climatic conditions, we ob-  
 375 serve important differences in both slopes for scenario SSP5-8.5, and also for scenario SSP3-7.0  
 376 and scenario SSP2-4.5, in the SAS.

377

378 **3.3 Active layer thickness evolution**

379 Numerical simulations provide access to the soil temperature at various depths. From the  
 380 soil temperature profile, the maximum depth with a positive temperature may be computed at each  
 381 time step. The maximum thawed depth obtained over a year defines the active layer thickness  
 382 (ALT) of this year. The active layer thickness has been computed for each scenario and each year  
 383 and is plotted for both the NAS and SAS in Figure 8.

384

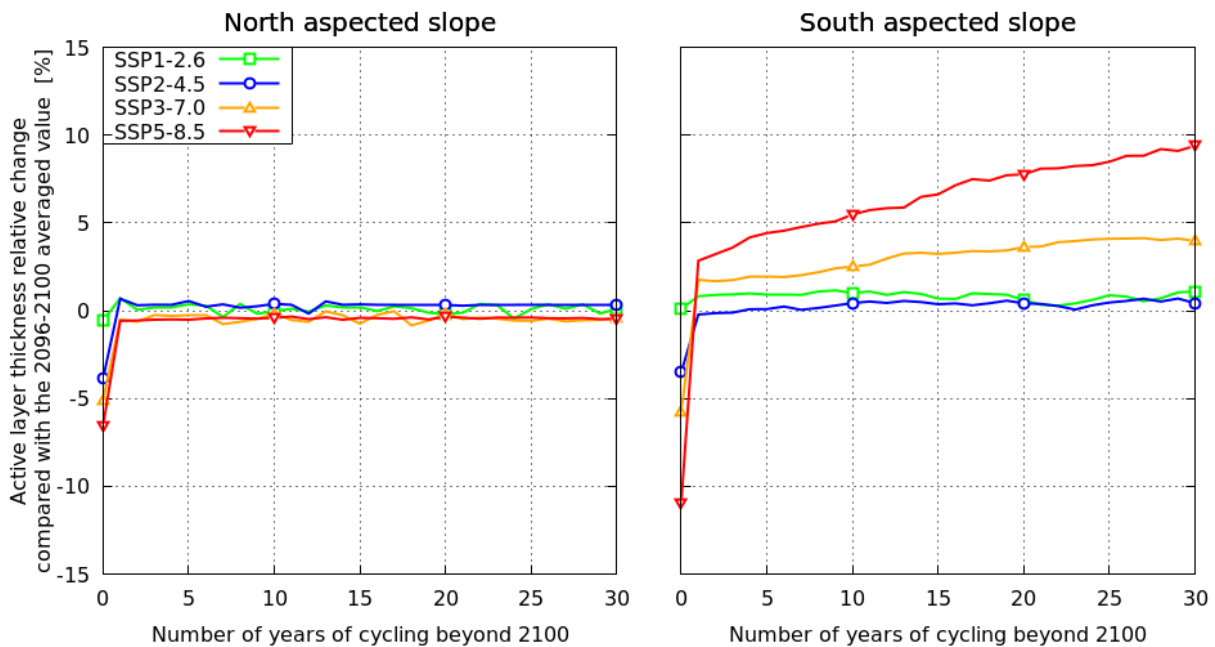


385 **Figure 8: Active layer thickness temporal evolution on the NAS (left) and SAS (right) of the**  
 386 **Kulingdakan watershed obtained from permaFoam simulations under different SSP scenar-**  
 387 **ios. Top : Active layer thickness value. Bottom : Relative change compared to 2014 value (63**  
 388 **cm for NAS, 100 cm for SAS).**  
 389

390

391 For both slopes, an increase in the active layer thickness is observed between 2014 and 2100 in every scenario, with a more important thickening in the SAS than in the NAS. SSP1-2.6 leads to an increase of +12.5 cm / +13% for the SAS and +8.8 cm / +14% for the NAS, while SSP5-8.5 leads to a more dramatic increase of +65.1 cm / +65% for the SAS and of +38.5 cm / +61% for the NAS. In the first half of the century, the behaviour of the active layer thickness does not differ significantly between scenarios, with a thickening rate in the ALT of about +3.6 mm/year ( $\pm 23\%$ ) in the SAS and +2.8 mm/year ( $\pm 18\%$ ) in the NAS. However, in the second half of the century (2050–2100), different scenarios lead to very different active layer thickness evolution dynamics. For SSP1-2.6, the thickening rate is rather small, with a rate of +0.60 mm/year for the SAS and +0.32 mm/year for the NAS, while for the SSP5-8.5 scenario, the thickening rate rises to +9.1 mm/year for the SAS and +5.1 mm/year for the NAS. By the end of the simulated period, these thickening rates show no diminishing trend in the SAS, suggesting that the dynamic thermal equilibrium is not reached in the active layer. To illustrate this, Figure 9 shows the active layer thickness evolution for 30 years of additional simulations while keeping the climatic conditions of the end of the century (2096–2100) for each scenario.

406



407

408 **Figure 9: Relative change in active layer thickness compared with the average value for 2096–**  
409 **2100 over 30 years of spin-up for a synthetic year obtained by averaging climatic conditions**  
410 **between 2096 and 2100.**

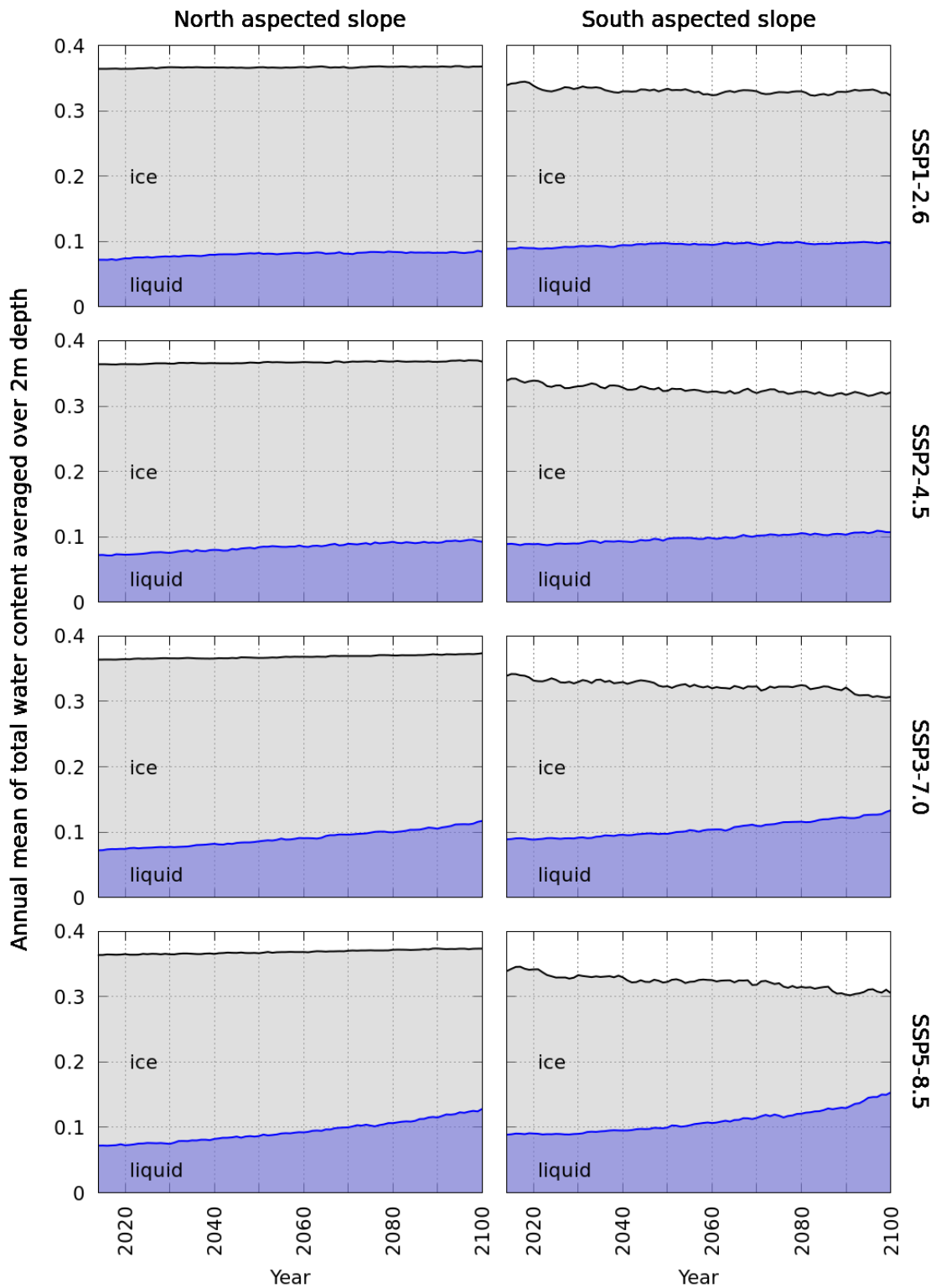
411

412 Overall, the active layer is not far from thermal equilibrium on both slopes for the low-forcing sus-  
413 tainable pathway (SSP1-2.6) and medium (SSP2-4.5) climatic scenarios. However, when consider-  
414 ing the high-forcing pathway SSP5-8.5 scenario, an important thermal inertia effect appears in the  
415 SAS, with an additional active layer thickness increase over these 30 years of +10.4 % compared to  
416 the 2096–2100 value, i.e. an increase of +17 cm. This additional change in the active layer thick-  
417 ness brings the resulting change compared to the 2014 value to +77 cm (+77%) for the SSP5-8.5  
418 scenario for the SAS. The abrupt change observed at the end of the first year of cycling is a direct  
419 observation of the abrupt change in climatic forcing (from 2100 forcings to 2096–2100 averaged  
420 conditions). Interannual variability is included in CMIP6 scenarios, as can be seen in Figure 2 for  
421 both the air temperature and precipitations. For the NAS, the active layer is back to equilibrium in a  
422 year, which is a sign of a short response time. For the SAS, and particularly for the steepest scenar-  
423 ios, this effect is added to a longer response time change, as discussed previously.

#### 424 **3.4 Trends in soil moisture**

425 The soil moisture content experienced less important changes than the thermal regime under  
426 the considered climate change scenario. To illustrate the soil moisture evolution near the surface,  
427 the total water, liquid water and ice volumetric contents have been averaged over the first 2 m of the  
428 soil for each slopes, and their 2014–2100 evolutions have been plotted in Figure 10 for the four cli-  
429 matic scenarios. Note that the 2 m surface soil layer thickness considered for this quantification en-  
430 compasses the entire area with water content evolution under the climate change scenarios. Regard-  
431 less of the scenario, there is no significant evolution of the total water content in the first 2 m of soil  
432 in the NAS, and the only noticeable change is the increase in the proportion of liquid water (+17%  
433 in SSP1-2.6, +28 % in SSP2-4.5, +62% in SSP3-7.0, +78% in SSP5-8.5), suggesting an increase in  
434 the amount of liquid water available for vegetation. In the SAS, however, the first 2 m of the soil  
435 exhibited a slight but detectable diminishing of the total water content by 2100 (-5 % in SSP1-2.6  
436 and SSP2-4.5, -10% in SSP3-7.0 and SSP5-8.5). On the other hand, the proportion of liquid water  
437 over ice increases (+9% in SSP1-2.6, +20% in SSP2-4.5, +50% in SSP3-7.0, +72% in SSP5-8.5).  
438 Therefore, on the SAS, climate warming may result in an increase in the amount of liquid water  
439 available for vegetation. This finding is important for heat and water transfers in the soil, given the  
440 strong couplings and non-linearities between these transfers. For instance, decreasing the total water  
441 content induces a decrease in the soil thermal inertia, while decreasing the share of ice versus liquid  
442 water induces a decrease in the apparent thermal conductivity. This can also impact the vegetation

443 dynamics, since vegetation takes up only liquid soil water for transpiration. It should be emphasised  
444 that the presented partitioning between liquid water and ice is based on the mean annual quantities.  
445 This provides a smaller proportion of liquid water compared to that at the end of the active season  
446 (second half of September), when the active layer is at its maximum thickness (see Supplementary  
447 material D).

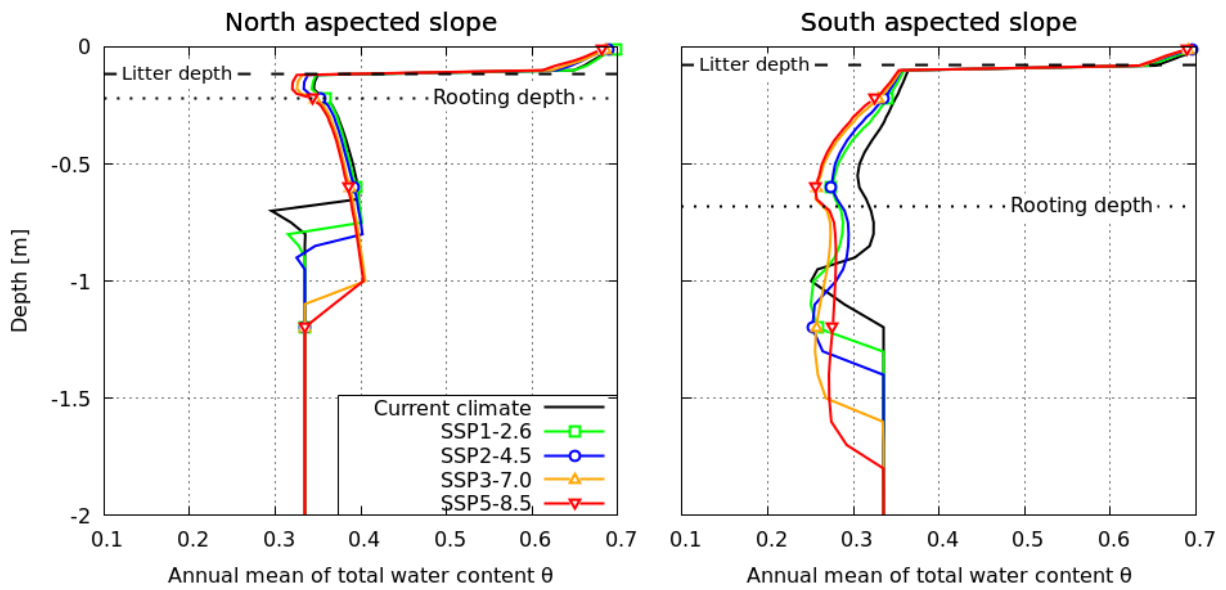


448

449 **Figure 10: Annual mean of total water content [m<sup>3</sup> of water / m<sup>3</sup> of soil] partitioned into liquid**  
 450 **(blue) and ice (grey) water content averaged over 2m depth in different climate projections.**

451

452 In order to investigate the local variation of the moisture content in the rooting zone and in  
453 the active layer of each slope, the vertical profiles of the mean annual total water content have been  
454 plotted in Figure 11 for current climatic conditions and for the year 2100 under the SSP1-2.6, SSP2-  
455 4.5, SSP3-7.0 and SSP5-8.5 scenarios. The processes driving the evolution of vertical moisture pro-  
456 files are complex; they involve coupled and non-linear heat and water transfers, as well as changing  
457 evapotranspiration fluxes. The main changes in the vertical moisture profiles can be described as  
458 follows. The water profiles do not change significantly in the highly porous organic horizon for  
459 both slopes. In the active layer within the mineral horizon, the behaviors of the SAS and NAS con-  
460 trast more. In most of the root layers of both slopes, upward vertical moisture gradients, and thus  
461 downward water movements, occur. This is likely the signature of an infiltration-dominated flow  
462 regime. On the contrary, below the root layer, there are downward vertical moisture gradients, and  
463 thus, according to the generalized Darcy's law, upward water movements. This could be explained  
464 by the root water uptake occurring above in the root layer, uptake that would create a capillarity-  
465 dominated zone where waters are attracted from the depth toward the root layer. SAS and NAS  
466 strongly differs in root layer thickness: 10 cm in the mineral horizon in NAS and 60 cm in the min-  
467 eral horizon in SAS. Then the shape of the profiles of vertical water fluxes strongly differs between  
468 the two slopes, as well as their response to climate change. In the NAS, the only evolution with cli-  
469 mate change is a thickening of the zone with a downward vertical moisture gradient (i.e. an upward  
470 water flux) alongside the thickening of the active layer, with no significant changes in the gradient  
471 itself. Meanwhile, in the SAS, along with the thickening of the zone with water movements (i.e.  
472 moisture gradients) that comes with active layer thickening, significant changes in the upward mois-  
473 ture gradients are expected to occur: the hotter the scenario, the steeper the gradients, and thus the  
474 stronger the downward water fluxes.



475

476 **Figure 11: Two-meter depth profiles of the annual mean of the total water content [ $\text{m}^3$  of wa-**  
 477 **ter /  $\text{m}^3$  of soil] in 2100: projections compared to current state.**

478

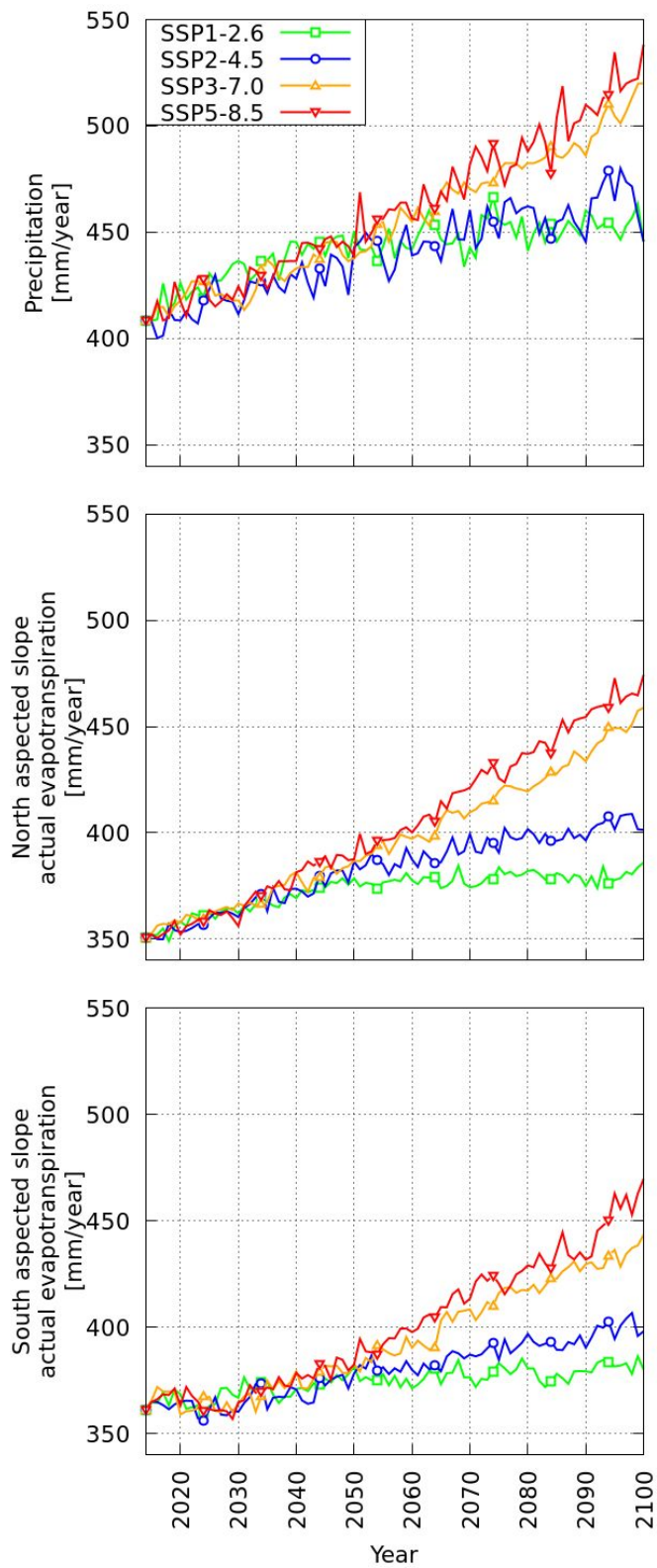
### 479 3.5 Water fluxes

480 The water fluxes also significantly change with climate change on both slopes for every sce-  
 481 nario. Evapotranspiration is the most important component of the hydrological budget in Kuling-  
 482 dakan. Focusing on this dominant component, Figure 12 presents the centennial evolution of evapo-  
 483 transpiration on both slopes and precipitation for the four climate change scenarios. A significant  
 484 increase in evapotranspiration is simulated in all cases, with an increase between +19 mm / +5%  
 485 (SSP1-2.6) and +108 mm / +30% (SSP5-8.5) in the SAS, and between +35mm / +10% and +123  
 486 mm / +35% in the NAS. The increase in the evapotranspiration fluxes in Kulingdakan is correlated  
 487 to the increase in precipitation, with similar rates for both slopes.

488

489





490

491 **Figure 12: Precipitation and actual evapotranspiration evolution over the century**

492 Similar to previous simulations of Mean Annual Temperature, soil surface temperature and Active  
493 Layer Thickness, the evolution is globally similar among scenarios until 2050, with significant di-  
494 vergences appearing only between 2050 and 2100.

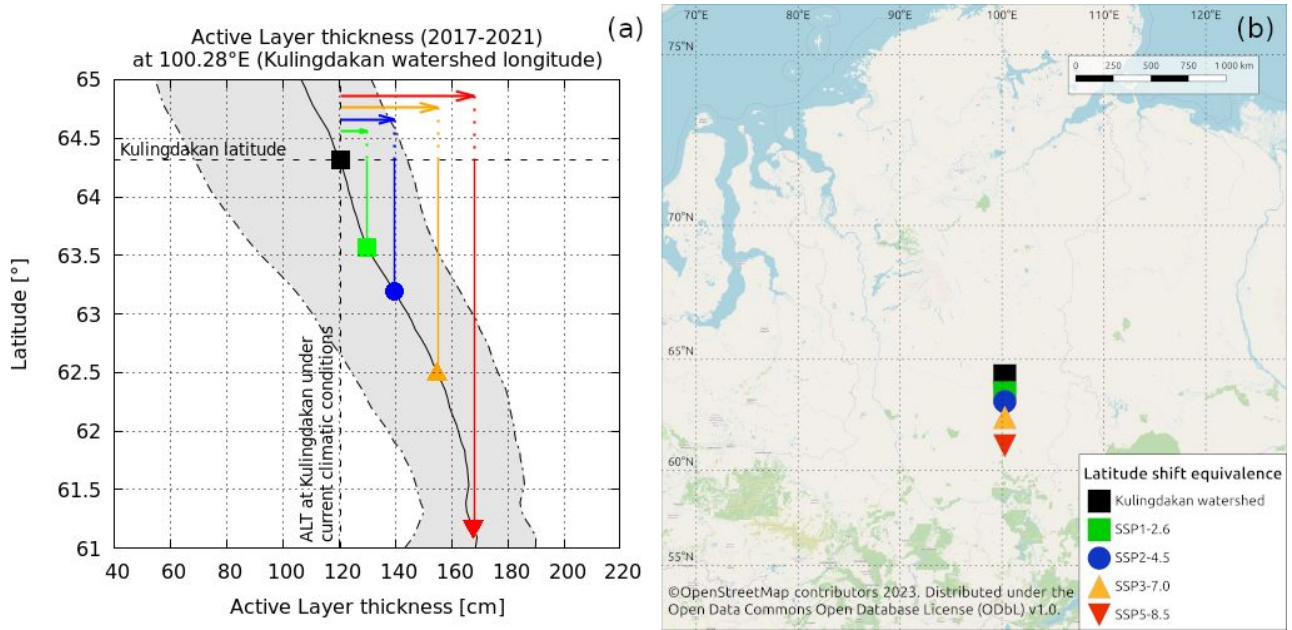
#### 495 **4 Discussion**

496 The numerical results obtained by the mechanistic modelling of heat and water transfer  
497 within the permafrost and active layer of Kulingdakan document the physical response to be ex-  
498 pected within this catchment under climate change, with soil warming (Fig. 6) and active layer  
499 thickening (Fig. 8) in all climate scenarios. An important spatial variability of this thermal response  
500 is identified, in relation with the aspect of the slopes, which stems from a sizable contrast in the  
501 vegetation cover, hydrologic and thermal state and active layer dynamics, as currently observed be-  
502 tween the two slopes of the catchment (Prokushkin et al, 2007). Indeed, since the NAS is wetter, its  
503 thermal inertia is more important due to the larger amount of latent heat that must be provided in or-  
504 der to thaw and warm its soils, compared to the drier soils of the SAS. This difference in moisture  
505 content is largely due to differences in the tree cover biomass and physiology. In particular, the  
506 deeper root layer in the SAS compared to the NAS induces more intensive evapotranspiration, un-  
507 der both current (Orgogozo et al., 2019) and future climate conditions. Note that this contrast be-  
508 tween the two slopes tends to diminish with climate warming (Fig. 12). Liquid water availability for  
509 root water uptake is better in SAS than in NAS under current climate as well as in the studied sce-  
510 narios of climate change (Supplementary Material D: A view of seasonal change of liquid water  
511 available for vegetation uptake). Meanwhile, the SAS is drier than the NAS in terms of total water  
512 content in current climate, and this contrast of dryness will increase with climate warming (Fig.  
513 10). The pattern of water fluxes within the active layer, with an upward flux to the thinner, close-to-  
514 the-surface root layer in the NAS and a downward flux toward the bottom of the thicker root layer  
515 in the SAS is also preserved under climate change, with an intensification of the fluxes in the SAS  
516 under the high forcing pathway scenarios (Fig. 11). According to Figure 11, the changes in vertical  
517 water fluxes will be stronger in the SAS than in NAS, likely due to the pronounced drying of the ac-  
518 tive layer of the SAS, while the total water content in the NAS does not change much (Fig. 10). The  
519 drying of the root layer in the SAS may then lead to steeper downward moisture gradient and thus  
520 more important infiltration flux within this layer. Furthermore, the thicker moss layer in the NAS is  
521 likely to alleviate more efficiently the effect of changes in the climatic conditions on soil compared  
522 to that in the SAS. Because our modelling takes into account the root water uptake mechanistically

523 (Orgogozo et al., 2023) and the low vegetation insulating effect empirically (Supplementary Mate-  
524 rial A – **Estimating soil surface temperature from external conditions**), the warming of the soil and  
525 the thickening of the active layer under climate change are significantly more pronounced in the  
526 SAS than in the NAS. This spatial variability in permafrost dynamics of forest environments, per-  
527 sistent at all climate change scenarios, reflects the prominent role of micro-climatic conditions in  
528 the responses to climate change that has been demonstrated recently in the literature (Zellweger et  
529 al., 2020). It must be emphasised that all the numerical results of this study have been obtained con-  
530 sidering the vegetation in its present state. The strong local variabilities of the vegetation cover de-  
531 pending on the permafrost conditions in the Kulingdakan catchment (Orgogozo et al., 2019) and,  
532 from a broader perspective, in the Arctic (Oehri et al., 2022), are consistent with the tight connec-  
533 tions between the evolution of vegetation under climate change (e.g. Vitasse et al. 2009, 2011; Rew  
534 et al., 2020) and the permafrost pattern, which has not been explicitly considered in this study. At  
535 the centennial time scale, changes in the tree growth rate, the forest fire frequency or the nature of  
536 the vegetation cover may exert important impacts on permafrost conditions (Cable et al., 2016; Fe-  
537 dorov et al., 2019; Rew et al., 2020; Li et al., 2021; Heijmans et al., 2022). Meanwhile, without be-  
538 littling these complex interactions between vegetation and permafrost dynamics, this study shows  
539 that important impacts of climate change on the permafrost dynamics of the forested continuous  
540 permafrost area are to be expected, even with the steady state of the vegetation. We noted that the  
541 more intense the climate change, the more pronounced these thermal responses. For instance, under  
542 the SSP5-8.5 scenario, a maximum evolution of the active layer thickness is +65 cm / +65% for the  
543 SAS and +39 cm / +61% for the NAS, while in the SSP2-4.5 scenario, an increase of +23 cm /  
544 +23% for the SAS and of +15 cm / +23% for the NAS is anticipated. Using empirical transfer func-  
545 tions to approximate the soil surface temperature from atmospheric conditions under climate change  
546 poses the problem of extrapolation, for instance under extreme hot weather conditions that may oc-  
547 cur in the future, which are unprecedented in the training period 1999–2014. However, performing  
548 the mechanistic modelling of the surface energy balance in extreme weather conditions under per-  
549 mafrost contexts was beyond the scope of this work. Additionally, it must be noted that for now in  
550 permaFoam, evapotranspiration is assumed to be solely constituted by transpiration, while the evap-  
551 oration within the soil is neglected (Orgogozo et al., 2019). This assumption is made in the context  
552 of the study of boreal forest areas, in which transpiration largely dominates over evaporation in the  
553 hydrological budget (e.g. Park et al., 2021). Meanwhile, evaporation may dominate in tundra envi-  
554 ronments (Clark et al., 2023) and likely to increase in the future in forested environments. Since soil

555 evaporation adds another coupling between heat and water transfers through exchanges of latent  
 556 heat, it could directly affect the soil temperature evolution. These points should constitute a scope  
 557 of future modelling works.

558 To produce a broader geographical context of the active layer thickening projections simu-  
 559 lated at the scale of a small catchment, a comparison of centennial evolutions under climate change  
 560 with large geographical coverage is performed using a substituting space for time approach (Fig.  
 561 13).



562

563 **Figure 13: (a) Equivalence between simulated active layer thickening by 2096–2100 under cli-**  
 564 **mate change (SAS and NAS average) and southward latitudinal shift in current climatic con-**  
 565 **ditions (2017–2021). – Latitudinal trend (black line – average over a 1°lat. × 1°long. poly-**  
 566 **gon) and envelope (in grey – min./max. over years within the same polygon) extracted from Per-**  
 567 **mafrost CCI (Westermann et al., 2024). (b) Representation of the latitudinal southward shift**  
 568 **equivalent to each climate scenario’s active layer thickening on the regional map.**

569

570 The simulated thickening of the active layer, averaged over both slopes of Kulingdakan, is depicted  
 571 as southward latitudinal shifts along the meridian passing by Kulingdakan, i.e. with a north-south  
 572 translation along 100.28 °E (Fig. 13). The latitudinal evolution of the active layer thickness along  
 573 the current meridian is computed based on the permafrost\_CCI dataset (Westermann et al., 2024)  
 574 by averaging the value of the multi-annual mean of the active layer thickness for the 2017–2021 pe-  
 575 riod over a polygon of 1° of latitude by 1° of longitude centred on the considered meridian and  
 576 browsing the latitude between 67°N and 57°N. The 1°-1° polygon was considered big enough to  
 577 smooth the small-scale non-homogeneities (at km scale) and small enough to capture the latitudinal

578 effect, including biome transitions (~hundreds of km, e.g. Anisimov et al., 2015) In Figure 13a, the  
579 black line describes the multi-annual (1997–2019) temporal average of the spatial average of the ac-  
580 tive layer thickness over a  $1^{\circ}$ - $1^{\circ}$  polygon centred on a moving latitude ; the grey shaded area repre-  
581 sents the minimum/maximum obtained for this spatial average during the considered period. It can  
582 be seen that, in the high-forcing pathway scenario SSP5-8.5, the active layer thickening would cor-  
583 respond to a 349 km southward shift, while in the medium scenario SSP2-4.5, it would correspond  
584 to a 124 km southward shift.

585 Under a permanently changing climatic context, an important question is the state of thermal  
586 equilibrium versus non-equilibrium of the permafrost (Obu et al., 2019): is the climate change in-  
587 duced warming slow enough that permafrost may be considered at every time close to the thermal  
588 equilibrium with climatic conditions, or on the contrary, do the transient effects dominate the ther-  
589 mal dynamics of permafrost under climate change? The simulation results of this work provide in-  
590 formation for characterising the degree of thermal equilibrium of the continuous permafrost, in a  
591 forested study site under various scenarios of climate change. First of all, we emphasise that, since  
592 the bottom thermal boundary condition in our modelling is the geothermal heat flux (Duchkov et  
593 al., 1997), the assumption of overall thermal equilibrium at depth (<10 m) in the hundreds of metres  
594 of the thick permafrost of the Putorana plateau (Pokrovsky et al., 2005) is implicitly made. Mean-  
595 while, the temperature profiles shown in Figure 7 demonstrate that under this assumption the ther-  
596 mal equilibrium state of the first 10 m of soil in 2100 depends on both the climate change scenario  
597 and the slope aspect. In the NAS, the thermal equilibrium of the first 10 m of soil is achieved by  
598 2100 in every climate scenario, with only a slight shift between the 2100 and (2100+30) conditions  
599 in the SSP5-8.5 scenario. Additionally, with sub-zero vertical thermal gradients in each scenario,  
600 only small heat exchanges between the surface and the deep layer may occur. On the contrary, by  
601 2100 in the SAS, strong thermal non-equilibrium is encountered in the two highforcing pathway  
602 scenarios, SSP3-7.0 and SSP5-8.5 (Fig. 7 and 8). Under these scenarios, sizable evolutions of tem-  
603 perature profiles are expected between 2100 and 2100+30. Moreover, for these two scenarios, the  
604 vertical thermal gradients between 1 and 10 m depth are clearly positive (considering an upward  
605 vertical axis), which implies an ongoing heat flux from the surface to the depths. In this case, the  
606 permafrost is warming below 10 m, at a rate that we implicitly assume to be small enough that it  
607 does not modify the total amount of heat stored within this deep permafrost. As such, in scenarios  
608 SSP3-7.0 and SSP5-8.5, the climate change clearly induces the transient warming of the permafrost  
609 below 10 m depth in the SAS of the Kulingdakan watershed. One could note slightly decreasing

610 trends in the soil temperature under scenarios SSP1-2.6 and SSP2-4.5. This is due to inter-annual  
611 variabilities in both the precipitation and air temperature in CMIP6 projections (Fig. 2). Therefore,  
612 the year 2100 may offer different conditions from those observed in the 2096-2100 average, which  
613 is repeated over 30 cycles to assess the equilibrium state of the permafrost,. For example, in SSP2-  
614 4.5, the last decade experiences an important annual precipitation peak, up to 475 mm/year, centred  
615 around 2095, before a decreasing trend in the second part of the decade, ending up with a precipita-  
616 tion of 410 mm/year projected in 2100. This results, for the year 2100, in a decrease in the snow  
617 cover insulating effect in winter and thus a lowering of the soil surface temperature (Fig. 5), com-  
618 pared to the conditions encountered in the previous decade.

619 Overall, the results of the present study may be used to improve our understanding of the  
620 climate-warming-related changes in the wide areas of boreal forest on continuous permafrost, with  
621 implications for continental surfaces (Revich et al., 2022), ecosystems (Wang and Liu 2022) and el-  
622 ement cycles (Schuur et al., 2022), and related global consequences and feedbacks. Mechanistic  
623 modelling, although it is computationally costly, is capable of providing quantitative information  
624 for these research fields. This approach should be applied in other environmentally monitored bo-  
625 real watershed, in order to numerically characterise the physical response of permafrost to climate  
626 change under various environmental contexts, for instance, in Northern Sweden (Auda et al., 2023)  
627 and Western Siberia (Cazaurang et al., 2023).

## 628 **5 Conclusion**

629 Four main conclusions that could be drawn from this numerical study are the following:

- 630 - All climate change scenarios trigger significant soil warming (+1.8°C in the SAS and +1.5°C in  
631 the NAS under the SSP2-4.5 scenario at 1 m depth according to the presented simulations) and an  
632 increase in the active layer thickness (+23 cm / +23% in the SAS and +15 cm / +23% in the NAS  
633 under the SSP2-4.5 scenario) for both slopes of the Kulingdakan watershed. The projected increase  
634 in the active layer thickness under the SSP2-4.5 scenario would be equivalent to a ~120 km south-  
635 ward shift in current climatic conditions, and to a ~350 km southward shift under the SSP5-8.5 sce-  
636 nario.
- 637 - For all climate change scenarios, the combination of soil warming and an increase in precipitation  
638 leads to an important increase in evapotranspiration for both slopes (+37 mm / +10% in the SAS  
639 and +51 mm / +14% in the NAS under the SSP2-4.5 scenario). Meanwhile, the mean annual soil  
640 moisture decreases only slightly in the NAS (-2.3% under the SSP2-4.5 scenario, averaged over the

641 22 cm of rooting depth), but the decrease is more pronounced in the SAS (-6.0% under the SSP2-  
642 4.5 scenario, averaged over the 68 cm of rooting depth).

643 - The important spatial variability observed in the Kulingdakan watershed illustrate the key role of  
644 meso-climatic conditions and small-scale geomorphological contrasts in the permafrost response to  
645 climate warming

646 - Under the two highforcing pathway scenarios of climate change, SSP3-7.0 and SSP5-8.5, the near-  
647 surface permafrost of the SAS of the Kulingdakan watershed is in a non-equilibrium thermal state  
648 in 2100, and further investigation is needed to assess whether or not the permafrost below 10 m  
649 depth will be close to thermal equilibrium in this region. This indicates the need to develop non-  
650 equilibrium modelling approaches for regional and global permafrost modelling under climate  
651 change.

652 The approach developed in this study can be applied to other high-latitude permafrost-affected  
653 catchments, provided that the necessary information on current thermal and hydrological parameters  
654 of the soil as well as vegetation coverage, is available.

655

## 656 **Competing interests**

657 The corresponding author has declared that none of the authors has any competing interests.

## 658 **Acknowledgments**

659 This work has been funded by the French National Research Agency ANR (grant no ANR-19  
660 CE46-0003-01) and benefited from access to the supercomputers of CALMIP (project p12166) and  
661 GENCI (project A0140410794, TGCC). This work was supported by a French government grant  
662 managed by the Agence Nationale de la Recherche under the ‘Investissements d’avenir’ program  
663 (reference ‘ANR-21-ESRE-0051’). Oleg Pokrovsky is grateful for partial support from the TSU De-  
664 velopment Programme PRIORITY – 2030 and project PEACE of PEPR FairCarboN ANR-22-  
665 PEXF-0011. Anatoly Prokushkin is supported by State Assignment no. 0287-2021-0008. Esteban  
666 Alonso Gonzalez is supported by the European Space Agency through the Climate Change Initia-  
667 tive postdoctoral grant.

668 **References**

669 Alonso-González, E., Aalstad, K., Baba, M. W., Revuelto, J., López-Moreno, J. I., Fiddes, J., Es-  
670 sery, R., and Gascoin, S.: The Multiple Snow Data Assimilation System (MuSA v1.0), *Geosci.*  
671 *Model Dev.*, 15, 9127–9155, <https://doi.org/10.5194/gmd-15-9127-2022>, 2022.

672

673 Anisimov, O. A., Zhiltcova, Y. L., and Razzhivin, V. Y.: Predictive modeling of plant productivity  
674 in the Russian Arctic using satellite data, *Izvestiya Atmospheric and Oceanic Physics*, 51(9), 1051–  
675 1059, <https://doi.org/10.1134/S0001433815090042>, 2015.

676

677 Arndal, M. F., and Topp-Jørgensen, E. (Eds.): INTERACT Station Catalogue – 2020, DCE – Dan-  
678 ish Centre for Environment and Energy, Aarhus University, Denmark, 190 pp., ISBN 978-87-  
679 93129-15-3, [www.eu-interact.org](http://www.eu-interact.org), 2020.

680

681 Auda, Y., Lundin, E. J., Gustafsson, J., Pokrovsky, O. S., Cazaurang, S., and Orgogozo, L.: A new  
682 land cover map of two watersheds under long-term environmental monitoring in the Swedish Arctic  
683 using Sentinel-2 data, *Water*, 15, 3311, <https://doi.org/10.3390/w15183311>, 2023.

684

685 Bartsch, A., Pointner, G., Nitze, I., Efimova, A., Jakober, D., Ley, S., Högström, E., Grosse, G., and  
686 Schweitzer, P.: Expanding infrastructure and growing anthropogenic impacts along Arctic coasts,  
687 *Environ. Res. Lett.*, 16, 115013, <https://doi.org/10.1088/1748-9326/ac3176>, 2021.

688

689 Blok, D., Heijmans, M. M. P. D., Schaepman-Strub, G., Van Ruijven, F., Parmentier, F. J. W., and  
690 Maximov, T. C.: The cooling capacity of mosses: Controls on water and energy fluxes in a Siberian  
691 tundra site, *Ecosystems*, 14, 1055–1065, <https://doi.org/10.1007/s10021-011-9463-5>, 2011.

692

693 Braithwaite, R. J., and Olesen, O. B.: Calculation of glacier ablation from air temperature, West  
694 Greenland, in: *Glacier Fluctuations and Climatic Change*, edited by: Oerlemans, J., Kluwer Aca-  
695 demic Publishers, 219–233, 1989.

696

697 Biskaborn, B. K., Smith, S. L., Noetzli, J., *et al.*: Permafrost is warming at a global scale, *Nat.*  
698 *Commun.*, 10, 264, <https://doi.org/10.1038/s41467-018-08240-4>, 2019.

699



700 Cable, W. L., Romanovsky, V. E., and Jorgenson, M. T.: Scaling-up permafrost thermal measure-  
701 ments in western Alaska using an ecotype approach, *The Cryosphere*, 10, 2517–2532, [https://](https://doi.org/10.5194/tc-10-2517-2016)  
702 [doi.org/10.5194/tc-10-2517-2016](https://doi.org/10.5194/tc-10-2517-2016), 2016.

703

704 Cazaurang, S., Marcoux, M., Pokrovsky, O. S., Loiko, S. V., Lim, A. G., Audry, S., Shirokova, L.  
705 S., and Orgogozo, L.: Numerical assessment of morphological and hydraulic properties of moss,  
706 lichen and peat from a permafrost peatland, *Hydrol. Earth Syst. Sci.*, 27, 431–451, [https://doi.org/](https://doi.org/10.5194/hess-27-431-2023)  
707 [10.5194/hess-27-431-2023](https://doi.org/10.5194/hess-27-431-2023), 2023.

708

709 Clark, J. A., Tape, K. D., and Young-Robertson, J. M., Quantifying evapotranspiration from domi-  
710 nant Arctic vegetation types using lysimeters, *Ecohydrology*, 16(1), e2484, 2023.

711

712 De Vrese, P., Georgievski, G., Gonzalez Rouco, J. F., Notz, D., Stacke, T., Steinert, N. J., Wilken-  
713 skjeld, S., and Brovkin, V.: Representation of soil hydrology in permafrost regions may explain  
714 large part of inter-model spread in simulated Arctic and subarctic climate, *The Cryosphere*, 17,  
715 2095–2118, <https://doi.org/10.5194/tc-17-2095-2023>, 2023.

716

717 Dominé, F., Fourteau, K., Picard, G., *et al.*: Permafrost cooled in winter by thermal bridging  
718 through snow-covered shrub branches, *Nat. Geosci.*, 15, 554–560, [https://doi.org/10.1038/s41561-](https://doi.org/10.1038/s41561-022-00979-2)  
719 [022-00979-2](https://doi.org/10.1038/s41561-022-00979-2), 2022.

720

721 Duchkov, A. D., Sokolova, L. S., Balobaev, V. T., Devyatkin, V. N., Kononov, V. I., and Lysak, S.  
722 V.: Heat flow and geothermal field in Siberia, *Geologiya / Geofizika*, 38(11), 1716–1729, 1997.

723

724 Essery, R.: A factorial snowpack model (FSM 1.0), *Geosci. Model Dev.*, 8, 3867–3876, [https://](https://doi.org/10.5194/gmd-8-3867-2015)  
725 [doi.org/10.5194/gmd-8-3867-2015](https://doi.org/10.5194/gmd-8-3867-2015), 2015.

726

727 Eyring, V., Bony, S., Meehl, G. A., Senior, C. A., Stevens, B., Stouffer, R. J., and Taylor, K. E.:  
728 Overview of the Coupled Model Intercomparison Project Phase 6 (CMIP6) experimental design and  
729 organization, *Geosci. Model Dev.*, 9, 1937–1958, <https://doi.org/10.5194/gmd-9-1937-2016>, 2016.

730

731 Fan, X., Duan, Q., Shen, C., Wu, Y., and Xing, C.: Global surface air temperatures in CMIP6: His-  
732 torical performance and future changes, *Environ. Res. Lett.*, 15, 104056, [https://doi.org/](https://doi.org/10.1088/1748-9326/abb051)  
733 10.1088/1748-9326/abb051, 2020.

734

735 Fedorov, A. N., Konstantinov, P. Y., Vasilyev, N. F., and Shestakova, A. A., The influence of bo-  
736 real forest dynamics on the current state of permafrost in Central Yakutia, *Polar Science*, 22,  
737 100483, <https://doi.org/10.1016/j.polar.2019.100483>, 2019.

738

739 Frolking, S.: Sensitivity of spruce/moss boreal forest net ecosystem productivity to seasonal anom-  
740 alies in weather, *Journal of Geophysical Research*, 102(D24), 29053–29064, [https://doi.org/](https://doi.org/10.1029/96JD03707)  
741 10.1029/96JD03707, 1997.

742

743 Gauthier, S., *et al.*: Boreal forest health and global change, *Science*, 349, 819–822, [https://doi.org/](https://doi.org/10.1126/science.aaa9092)  
744 10.1126/science.aaa9092, 2015.

745

746 Gentsch, N.: *Permafrost Soils in Central Siberia: Landscape Controls on Soil Organic Carbon Stor-*  
747 *age in a Light Taiga Biome*, Akademische Verlagsgemeinschaft München, Munich, Germany,  
748 2011.

749

750 Haesen, S., Lembrechts, J. J., De Frenne, P., Lenoir, J., Aalto, J., Ashcroft, M. B., Kopecký, M.,  
751 Luoto, M., Maclean, I., Nijs, I., Niittynen, P., van den Hoogen, J., Arriga, N., Brúna, J., Buchmann,  
752 N., Čiliak, M., Collalti, A., De Lombaerde, E., Descombes, P., ... Van Meerbeek, K.: ForestTemp –  
753 Sub-canopy microclimate temperatures of European forests, *Global Change Biology*, 27, 6307–  
754 6319, <https://doi.org/10.1111/gcb.15892>, 2021.

755

756 Hamm, A., and Frampton, A.: Impact of lateral groundwater flow on hydrothermal conditions of the  
757 active layer in a high-Arctic hillslope setting, *The Cryosphere*, 15, 4853–4871, [https://doi.org/](https://doi.org/10.5194/tc-15-4853-2021)  
758 10.5194/tc-15-4853-2021, 2021.

759

760 Hamon, W.R.: Computation of direct runoff amounts from storm rainfall, *International Association*  
761 *of Scientific Hydrological Sciences Publication*, 63, 52–62, 1963.

762

763 Heijmans, M. M. P. D., Magnússon, R. Í. Lara, M. J., *et al.*: Tundra vegetation change and impacts  
764 on permafrost, *Nat. Rev. Earth Environ.*, 3, 68–84, <https://doi.org/10.1038/s43017-021-00233-0>,  
765 2022.

766

767 Hersbach, H., Bell, B., Berrisford, P., Hirahara, S., Horányi, A., Muñoz-Sabater, J., Nicolas, J., Peu-  
768 bey, C., Radu, R., Schepers, D., Simmons, A., Soci, C., Abdalla, S., Abellan, X., Balsamo, G.,  
769 Bechtold, P., Biavati, G., Bidlot, J., Bonavita, M., De Chiara, G., Dahlgren, P., Dee, D., Diamanta-  
770 kis, M., Dragani, R., Flemming, J., Forbes, R., Fuentes, M., Geer, A., Haimberger, L., Healy, S.,  
771 Hogan, R. J., Hólm, E., Janisková, M., Keeley, S., Laloyaux, P., Lopez, P., Lupu, C., Radnoti, G.,  
772 de Rosnay, P., Rozum, I., Vamborg, F., Villaume, S., and Thépaut, J.-N.: The ERA5 global reanaly-  
773 sis, *Q. J. Roy. Meteor. Soc.*, 146, 1999–2049, <https://doi.org/10.1002/qj.3803>, 2020.

774

775 Hjort, J., Karjalainen, O., Aalto, J., *et al.*: Degrading permafrost puts Arctic infrastructure at risk by  
776 mid-century, *Nat. Commun.*, 9, 5147, <https://doi.org/10.1038/s41467-018-07557-4>, 2018.

777

778 Hjort, J., Streletskiy, D., Doré, G., *et al.*: Impacts of permafrost degradation on infrastructure, *Nat.*  
779 *Rev. Earth Environ.*, 3, 24–38, <https://doi.org/10.1038/s43017-021-00247-8>, 2022.

780

781 Hock, R.: Temperature index melt modelling in mountain areas, *Journal of Hydrology*, 282(1–4),  
782 104–115, [https://doi.org/10.1016/S0022-1694\(03\)00257-9](https://doi.org/10.1016/S0022-1694(03)00257-9), 2003.

783

784 Holloway, J. E., Lewkowicz, A. G., Douglas, T. A., *et al.* : Impact of wildfire on permafrost land-  
785 scapes: A review of recent advances and future prospects, *Permafrost and Periglac. Process.*, 31,  
786 371–382, <https://doi.org/10.1002/ppp.2048>, 2020.

787

788 Hu, G., Zhao, L., Wu, T., Wu, X., Park, H., Li, R., *et al.*: Continued warming of the permafrost re-  
789 gions over the Northern Hemisphere under future climate change, *Earth’s Future*, 10,  
790 e2022EF002835, <https://doi.org/10.1029/2022EF002835>, 2022.

791

792 Hu, G., Zhao, L., Li, R., Park, H., Wu, X., Su, Y., Guggenberger, G., Wu, T., Zou, D., Zhu, X.,  
793 Zhang, W., Wu, Y., and Hao, J.: Water and heat coupling processes and its simulation in frozen

794 soils: Current status and future research directions, *CATENA*, 222, 106844, ISSN 0341-8162,  
795 <https://doi.org/10.1016/j.catena.2022.106844>, 2023  
796

797 Iturbide, M., Fernández, J., Gutiérrez, J. M., Bedia, J., Cimadevilla, E., Díez-Sierra, J., Manzanas,  
798 R., Casanueva, A., Baño-Medina, J., Milovac, J., Herrera, S., Cofiño, A. S., San Martín, D., García-  
799 Díez, M., Hauser, M., Huard, D., and Yelekci, Ö.: Repository supporting the implementation of  
800 FAIR principles in the IPCC-WG1 Atlas, Zenodo, <https://doi.org/10.5281/zenodo.3691645>,  
801 <https://github.com/IPCC-WG1/Atlas>, 2022.  
802

803 Jan, A., and Painter, S. L.: Permafrost thermal conditions are sensitive to shifts in snow timing, *En-  
804 viron. Res. Lett.*, 15, 084026, 2020.  
805

806 Jan, A.: Modeling the role of lateral surface flow in low-relief polygonal tundra, *Permafrost and  
807 Periglac. Process.*, 33(3), 214–225, <https://doi.org/10.1002/ppp.2145>, 2022.  
808

809 Ji, H., Nan, Z., Hu, J., Zhao, Y., and Zhang, Y.: On the spin-up strategy for spatial modeling of per-  
810 mafrost dynamics: A case study on the Qinghai-Tibet Plateau, *Journal of Advances in Modeling  
811 Earth Systems*, 14, e2021MS002750, <https://doi.org/10.1029/2021MS002750>, 2022.  
812

813 Jin, H., Huang, Y., Bense, V. F., Ma, Q., Marchenko, S. S., Shepelev, V. V., Hu, Y., Liang, S.,  
814 Spektor, V. V., Jin, X., *et al.*: Permafrost degradation and its hydrogeological impacts, *Water*, 14,  
815 372, <https://doi.org/10.3390/w14030372>, 2022.  
816

817 Karjalainen, O., Aalto, J., Luoto, M., *et al.*: Circumpolar permafrost maps and geohazard indices for  
818 near-future infrastructure risk assessments, *Sci. Data*, 6, 190037, [https://doi.org/10.1038/  
819 sdata.2019.37](https://doi.org/10.1038/sdata.2019.37), 2019.  
820

821 Karlsson, J., Serikova, S., Vorobyev, S. N., *et al.*: Carbon emission from Western Siberian inland  
822 waters. *Nat. Commun.*, 12, 825, <https://doi.org/10.1038/s41467-021-21054-1>, 2021.  
823

824 Kim, J.-S., *et al.*: Extensive fires in southeastern Siberian permafrost linked to preceding Arctic Os-  
825 cillation, *Sci. Adv.*, 6, eaax3308, <https://doi.org/10.1126/sciadv.aax3308>, 2020.

826

827 Kirdyanov, A.V., Saurer, M., Siegwolf, R., Knorre, A. A., Prokushkin, A. S., Churakova  
828 (Sidorova), O. V., Fonti M. V., and Büntgen, U.: Long-term ecological consequences of forest fires  
829 in the continuous permafrost zone of Siberia, *Environ. Res. Lett.*, 15, 034061, 2020.

830

831 Kirdyanov, A.V., Saurer, M., Arzac, A., Knorre, A. A., Prokushkin, A. S., Churakova (Sidorova),  
832 O. V., Arosio, T., Bebhuk, T., Siegwolf, R., and Büntgen, U.: Thawing permafrost can mitigate  
833 warming-induced drought stress in boreal forest trees, *Science of the Total Environment*, 912,  
834 168858, ISSN 0048-9697, <https://doi.org/10.1016/j.scitotenv.2023.168858>, 2024.

835

836 Khani, H. M., Kinnard, C., Gascoin, S., and Lévesque, E.: Fine-scale environment control on  
837 ground surface temperature and thaw depth in a High Arctic tundra landscape, *Permafrost and*  
838 *Periglac. Process.*, 34(4), 467–480, <https://doi.org/10.1002/ppp.2203>, 2023.

839

840 Kurylyk, B. L., and Watanabe, K.: The mathematical representation of freezing and thawing pro-  
841 cesses in variably-saturated, non-deformable soils, *Advances in Water Resources*, 60, 160–177,  
842 ISSN 0309-1708, <https://doi.org/10.1016/j.advwatres.2013.07.016>, 2013.

843

844 Kurylyk, B. L.: Engineering challenges of warming, *Nat. Clim. Chang.*, 9, 807–808, <https://doi.org/10.1038/s41558-019-0612-8>, 2019.

846

847 Lamontagne-Hallé, P., McKenzie, J. M., Kurylyk, B. L., and Zipper, S.C.: Changing groundwater  
848 discharge dynamics in permafrost regions, *Environ. Res. Lett.*, 13, 084017, 2018.

849

850 Li, X.-Y., Jin, H.-J., Wang, H.-W., Marchenko, S. S., Shan, W., Luo, D.-L., He, R.-X., Spektor, V.,  
851 Huang, Y.-D., Li, X.-Y., and Jia, N.: Influences of forest fires on the permafrost environment: A re-  
852 view, *Advances in Climate Change Research*, 12(1), 48–65, ISSN 1674-9278, <https://doi.org/10.1016/j.accre.2021.01.001>, 2021.

854

855 Li, G., Zhang, M., Pei, W., Melnikov, A., Khristoforov, I., Li, R., and Yu, F.: Changes in per-  
856 mafrost extent and active layer thickness in the Northern Hemisphere from 1969 to 2018, *Science of*

857 the Total Environment, 804, 150182, ISSN 0048-9697, <https://doi.org/10.1016/>  
858 [j.scitotenv.2021.150182](https://doi.org/10.1016/j.scitotenv.2021.150182), 2022a.

859

860 Li, C., Wei, Y., Liu, Y., Li, L., Peng, L., Chen, J., *et al.*: Active layer thickness in the Northern  
861 Hemisphere: Changes from 2000 to 2018 and future simulations, *Journal of Geophysical Research:*  
862 *Atmospheres*, 127, e2022JD036785, <https://doi.org/10.1029/2022JD036785>, 2022b.

863

864 Loranty, M. M., Abbott, B. W., Blok, D., Douglas, T. A., Epstein, H. E., Forbes, B. C., Jones, B.  
865 M., Kholodov, A. L., Kropp, H., Malhotra, A., Mamet, S. D., Myers-Smith, I. H., Natali, S. M.,  
866 O'Donnell, J. A., Phoenix, G. K., Rocha, A. V., Sonnentag, O., Tape, K. D., and Walker, D. A.: Re-  
867 views and syntheses: Changing ecosystem influences on soil thermal regimes in northern high-lati-  
868 tude permafrost regions, *Biogeosciences*, 15, 5287–5313, <https://doi.org/10.5194/bg-15-5287-2018>,  
869 2018.

870

871 Makarieva, O., Nesterova, N., Post, D. A., Sherstyukov, A., and Lebedeva, L.: Warming tempera-  
872 tures are impacting the hydrometeorological regime of Russian rivers in the zone of continuous per-  
873 mafrost, *The Cryosphere*, 13, 1635–1659, <https://doi.org/10.5194/tc-13-1635-2019>, 2019.

874

875 Mashukov, D. A., Benkova, A. V., Benkova, V. E., *et al.*: Radial growth and anatomic structure of  
876 the trunk wood of healthy and stag-headed larch trees on permafrost, *Contemp. Probl. Ecol.*, 14,  
877 767–774, <https://doi.org/10.1134/S1995425521070143>, 2021.

878

879 Miner, K. R., Turetsky, M. R., Malina, E., *et al.*: Permafrost carbon emissions in a changing Arctic,  
880 *Nat. Rev. Earth Environ.*, 3, 55–67, <https://doi.org/10.1038/s43017-021-00230-3>, 2022.

881

882 Nitzbon, J., Krinner, G., Schneider von Deimling, T., Werner, M., and Langer, M.: First quantifica-  
883 tion of the permafrost heat sink in the Earth's climate system, *Geophysical Research Letters*, 50,  
884 e2022GL102053, <https://doi.org/10.1029/2022GL102053>, 2023.

885

886 Nitze, I., Grosse, G., Jones, B. M., *et al.*: Remote sensing quantifies widespread abundance of per-  
887 mafrost region disturbances across the Arctic and Subarctic, *Nat. Commun.*, 9, 5423, [https://](https://doi.org/10.1038/s41467-018-07663-3)  
888 [doi.org/10.1038/s41467-018-07663-3](https://doi.org/10.1038/s41467-018-07663-3), 2018.

889

890 Obu, J., Westermann, S., Bartsch, A., Berdnikov, N., Christiansen, H. H., Dashtseren, A., Delaloye,  
891 R., Elberling, B., Etzelmüller, B., Kholodov, A., Khomutov, A., Kääb, A., Leibman, M. O.,  
892 Lewkowicz, A. G., Panda, S. K., Romanovsky, V., Way, R. G., Westergaard-Nielsen, A., Wu, T.,  
893 Yamkhin, J., and Zou, D., Northern Hemisphere permafrost map based on TTOP modelling for  
894 2000–2016 at 1 km<sup>2</sup> scale, *Earth-Science Reviews*, 193, 299–316, ISSN 0012-8252, [https://](https://doi.org/10.1016/j.earscirev.2019.04.023)  
895 [doi.org/10.1016/j.earscirev.2019.04.023](https://doi.org/10.1016/j.earscirev.2019.04.023), 2019.

896

897 Oehri, J., Schaepman-Strub, G., Kim, J. S., *et al.*: Vegetation type is an important predictor of the  
898 arctic summer land surface energy budget, *Nat. Commun.*, 13, 6379, [https://doi.org/10.1038/](https://doi.org/10.1038/s41467-022-34049-3)  
899 [s41467-022-34049-3](https://doi.org/10.1038/s41467-022-34049-3), 2022.

900

901 O’Neill, B. C., Tebaldi, C., van Vuuren, D. P., Eyring, V., Friedlingstein, P., Hurtt, G., Knutti, R.,  
902 Kriegler, E., Lamarque, J.-F., Lowe, J., Meehl, G. A., Moss, R., Riahi, K., and Sanderson, B. M.:  
903 The Scenario Model Intercomparison Project (ScenarioMIP) for CMIP6, *Geosci. Model Dev.*, 9,  
904 3461–3482, <https://doi.org/10.5194/gmd-9-3461-2016>, 2016.

905

906 Orgogozo, L., Prokushkin, A. S., Pokrovsky, O. S., Grenier, C., Quintard, M., Viers, J., and Audry,  
907 S.: Water and energy transfer modeling in a permafrost-dominated, forested catchment of Central  
908 Siberia: The key role of rooting depth, *Permafrost and Periglacial Processes*, 30, 75–89, [https://](https://doi.org/10.1002/ppp.1995)  
909 [doi.org/10.1002/ppp.1995](https://doi.org/10.1002/ppp.1995), 2019.

910

911 Orgogozo, L., Xavier, T., Oulbani, H., and Grenier, C.: Permafrost modelling with OpenFOAM®:  
912 New advancements of the permaFoam solver, *Computer Physics Communications*, 282, [https://](https://doi.org/10.1016/j.cpc.2022.108541)  
913 [doi.org/10.1016/j.cpc.2022.108541](https://doi.org/10.1016/j.cpc.2022.108541), 2023.

914

915 Park, H., Tanoue, M., Sugimoto, A., Ichiyanagi, K., Iwahana, G., and Hiyama, T.: Quantitative sep-  
916 aration of precipitation and permafrost waters used for evapotranspiration in a boreal forest: A nu-  
917 merical study using tracer model, *Journal of Geophysical Research: Biogeosciences*, 126,  
918 e2021JG006645, <https://doi.org/10.1029/2021JG006645>, 2021.

919

920 Park, S. W., Kim, J. S., and Kug, J. S.: The intensification of Arctic warming as a result of CO<sub>2</sub>  
921 physiological forcing, *Nat. Commun.*, 11, 2098, <https://doi.org/10.1038/s41467-020-15924-3>, 2020.  
922

923 Park, S. W., and Kug, J. S.: A decline in atmospheric CO<sub>2</sub> levels under negative emissions may en-  
924 hance carbon retention in the terrestrial biosphere, *Commun. Earth Environ.*, 3, 289, [https://](https://doi.org/10.1038/s43247-022-00621-4)  
925 [doi.org/10.1038/s43247-022-00621-4](https://doi.org/10.1038/s43247-022-00621-4), 2022.  
926

927 Pokrovsky, O. S., Schott, J. S., Kudryavtzev, D. I., and Dupré, B.: Basalt weathering in Central  
928 Siberia under permafrost conditions, *Geochimica et Cosmochimica Acta*, 69(24), 5659–5680, 2005.  
929

930 Porter, C., Howat, I., Noh, M.-J., Husby, E., Khuvis, S., Danish, E., Tomko, K., Gardiner, J., Ne-  
931 grete, A., Yadav, B., Klassen, J., Kelleher, C., Cloutier, M., Bakker, J., Enos, J., Arnold, G., Bauer,  
932 G., and Morin, P., ArcticDEM - Mosaics, Version 4.1, Harvard Dataverse, V1, [https://doi.org/](https://doi.org/10.7910/DVN/3VDC4W)  
933 [10.7910/DVN/3VDC4W](https://doi.org/10.7910/DVN/3VDC4W), 2023.  
934

935 Prokushkin, A., Kajimoto, T., Prokushkin, S., McDowell, W., Abaimov, A. P., and Matsuura, Y.:  
936 Climatic factors influencing fluxes of dissolved organic carbon from the forest floor in a continu-  
937 ous-permafrost Siberian watershed, *Canadian Journal of Forest Research-Journal Canadien de la*  
938 *Recherche Forestiere*, 35, 2130–2140, <https://doi.org/10.1139/x05-150>, 2004.  
939

940 Prokushkin, A. S., Gleixner, G., McDowell, W. H., Ruehlow, S., and Schulze, E.-D.: Source- and  
941 substrate-specific export of dissolved organic matter from permafrost-dominated forested watershed  
942 in central Siberia, *Global Biogeochem. Cycles*, 21, GB4003, [https://doi.org/](https://doi.org/10.1029/2007GB002938)  
943 [10.1029/2007GB002938](https://doi.org/10.1029/2007GB002938), 2007.  
944

945 Ramage, J., Jungsberg, L., Wang, S., *et al.*: Population living on permafrost in the Arctic, *Popul.*  
946 *Environ.*, 43, 22–38, <https://doi.org/10.1007/s11111-020-00370-6>, 2021.  
947

948 Revich, B. A., Eliseev, D. O., and Shaposhnikov, D. A.: Risks for public health and social infra-  
949 structure in Russian Arctic under climate change and permafrost degradation, *Atmosphere*, 13, 532,  
950 <https://doi.org/10.3390/atmos13040532>, 2022.  
951



952 Rew, L. J., McDougall, K. L., Alexander, J. M., Daehler, C. C., Essl, F., Haider, S., Kueffer, C.,  
953 Lenoir, J., Milbau, A., Nuñez, M. A., Pauchard, A., and Rabitsch, W.: Moving up and over: Redis-  
954 tribution of plants in alpine, Arctic, and Antarctic ecosystems under global change, *Arctic, Antarc-*  
955 *tic, and Alpine Research*, 52(1), 651–665, <https://doi.org/10.1080/15230430.2020.1845919>, 2020.

956

957 Schneider von Deimling, T., Lee, H., Ingeman-Nielsen, T., Westermann, S., Romanovsky, V., Lam-  
958 oureux, S., Walker, D. A., Chadburn, S., Trochim, E., Cai, L., Nitzbon, J., Jacobi, S., and Langer,  
959 M.: Consequences of permafrost degradation for Arctic infrastructure – bridging the model gap be-  
960 tween regional and engineering scales, *The Cryosphere*, 15, 2451–2471, [https://doi.org/10.5194/tc-](https://doi.org/10.5194/tc-15-2451-2021)  
961 [15-2451-2021](https://doi.org/10.5194/tc-15-2451-2021), 2021.

962

963 Schuur, E.A.G., *et al.*: Permafrost and climate change: Carbon cycle feedbacks from the warming  
964 Arctic, *Annual Review of Environment and Resources*, 47(1), 343–371, 2022.

965

966 Shiklomanov, N. I., Streletskiy, D. A., Swales, T. B., and Kokorev, V. A.: Climate change and sta-  
967 bility of urban infrastructure in Russian permafrost regions: Prognostic assessment based on GCM  
968 climate projections, *Geographical Review*, 107(1), 125–142, <https://doi.org/10.1111/gere.12214>,  
969 2017.

970

971 Sjöberg, Y., Coon, E., Sannel, A. B. K., Pannetier, R., Harp, D., Frampton, A., Painter, S. L., and  
972 Lyon, S. W.: Thermal effects of groundwater flow through subarctic fens: A case study based on  
973 field observations and numerical modeling, *Water Resour. Res.*, 52, 1591–1606, [https://doi.org/](https://doi.org/10.1002/2015WR017571)  
974 [10.1002/2015WR017571](https://doi.org/10.1002/2015WR017571), 2016.

975

976 Sonke, J. E., Teisserenc, R., Heimbürger-Boavida, L.-E., Petrova, M. V., Maruszczak, N., Le Dantec,  
977 T., Chupakov, A. V., Li, C., Thackray, C. P., Sunderland, E. M., Tananaev, N., and Pokrovsky, O.  
978 S.: Eurasian river spring flood observations support net Arctic Ocean mercury export to the atmos-  
979 phere and Atlantic Ocean, *PNAS*, 115, 50, E11586–E11594, [www.pnas.org/cgi/doi/10.1073/](http://www.pnas.org/cgi/doi/10.1073/pnas.1811957115)  
980 [pnas.1811957115](http://www.pnas.org/cgi/doi/10.1073/pnas.1811957115), 2018.

981

982 Speetjens, N. J., Hugelius, G., Gumbrecht, T., Lantuit, H., Berghuijs, W. R., Pika, P. A., Poste, A.,  
983 and Vonk, J. E.: The pan-Arctic catchment database (ARCADE), *Earth Syst. Sci. Data*, 15, 541–  
984 554, <https://doi.org/10.5194/essd-15-541-2023>, 2023.

985

986 Streletskiy, D. A., Suter, L. J., Shiklomanov, N. I., Porfiriev, B. N., and Eliseev, D. O.: Assessment  
987 of climate change impacts on buildings, structures and infrastructure in the Russian regions on per-  
988 mafrost, *Environ. Res. Lett.*, 14, 025003, 2019.

989  
990 Streletskiy, D. A., Clemens, S., Lanckman, J.-P., and Shiklomanov, N. I.: The costs of Arctic infra-  
991 structure damages due to permafrost degradation, *Environ. Res. Lett.*, 18, 015006, [https://doi.org/](https://doi.org/10.1088/1748-9326/acab18)  
992 10.1088/1748-9326/acab18, 2023.

993  
994 Stuenzi, S. M., Boike, J., Gädeke, A., Herzsuh, U., Kruse, S., Pestryakova, L. A., Westermann,  
995 S., and Langer, M.: Sensitivity of ecosystem-protected permafrost under changing boreal forest  
996 structures, *Environ. Res. Lett.*, 16, 084045, <https://doi.org/10.1088/1748-9326/ac153d>, 2021.

997  
998 van Vuuren, D. P., Edmonds, J., Thomson, A., Riahi, K., Kainuma, M., Matsui, T., Hurtt, G. C.,  
999 Lamarque, J.-F., Meinshausen, M., Smith, S., Granier, C., Rose, S. K., and Hibbard, K. A.: The rep-  
1000 resentative concentration pathways: An overview, *Climatic Change*, 109, 5–31, [https://doi.org/](https://doi.org/10.1007/s10584-011-0148-z)  
1001 10.1007/s10584-011-0148-z, 2011.

1002  
1003 Viers, J., Prokushkin, A. S., Pokrovsky, O. S., *et al.*: Seasonal and spatial variability of elemental  
1004 concentrations in boreal forest larch foliage of Central Siberia on continuous permafrost, *Biogeo-*  
1005 *chemistry*, 113(1-3), 435–449, <https://doi.org/10.1007/s10533-012-9770-8>, 2013.

1006  
1007 Vitasse, Y., Porté, A. J., Kremer, A., *et al.*: Responses of canopy duration to temperature changes in  
1008 four temperate tree species: Relative contributions of spring and autumn leaf phenology, *Oecologia*,  
1009 161, 187–198, <https://doi.org/10.1007/s00442-009-1363-4>, 2009.

1010  
1011 Vitasse, Y., François, C., Delpierre, N., Dufrêne, E., Kremer, A., Chuine, I., and Delzon S.: Assess-  
1012 ing the effects of climate change on the phenology of European temperate trees, *Agricultural and*  
1013 *Forest Meteorology*, 151(7), 969–980, ISSN 0168-1923, [https://doi.org/10.1016/](https://doi.org/10.1016/j.agrformet.2011.03.003)  
1014 [j.agrformet.2011.03.003](https://doi.org/10.1016/j.agrformet.2011.03.003), 2011.

1015  
1016 Vonk, J. E., Speetjens, N. J., and Poste, A. E.: Small watersheds may play a disproportionate role in  
1017 arctic land-ocean fluxes, *Nat. Commun.*, 14, 3442, <https://doi.org/10.1038/s41467-023-39209-7>,  
1018 2023.

1019  
1020 Walvoord, M. A., and Kurylyk, B. L.: Hydrologic impacts of thawing permafrost—A review, *Va-*  
1021 *dose Zone Journal*, 15, 1–20, <https://doi.org/10.2136/vzj2016.01.0010>, 2016.

1023 Walvoord, M. A., and Striegl, R. G.: Complex vulnerabilities of the water and aquatic carbon cycles  
1024 to permafrost thaw, *Front. Clim.*, 3, 730402, <https://doi.org/10.3389/fclim.2021.730402>, 2021.  
1025

1026 Wang, J., and Liu, D.: Vegetation green-up date is more sensitive to permafrost degradation than  
1027 climate change in spring across the northern permafrost region, *Global Change Biology*, 28, 1569–  
1028 1582, <https://doi.org/10.1111/gcb.16011>, 2022.  
1029

1030 Weller, H. G., Tabor, G., Jasak, H., and Fureby, C.: A tensorial approach to computational contin-  
1031 uum mechanics using object orientated techniques, *Computers in Physics*, 12, 620–631, <https://doi.org/10.1063/1.168744>, 1998.  
1032  
1033

1034 Westermann, S., Barboux, C., Bartsch, A., Delaloye, R., Grosse, G., Heim, B., Hugelius, G., Irr-  
1035 gang, A., Kääh, A. M., Matthes, H., Nitze, I., Pellet, C., Seifert, F. M., Strozzi, T., Wegmüller, U.,  
1036 Wieczorek, M., and Wiesmann, A.: ESA Permafrost Climate Change Initiative (Permafrost\_cci):  
1037 Permafrost active layer thickness for the Northern Hemisphere, v4.0, NERC EDS Centre for Envi-  
1038 ronmental Data Analysis, 24 April 2024, <https://doi.org/10.5285/d34330ce3f604e368c06d76de1987ce5>, 2024.  
1039  
1040

1041 Wright, S. N., Thompson, L. M., Olefeldt, D., Connon, R. F., Carpino, O. A., Beel, C. R., and Quin-  
1042 ton, W. L.: Thaw-induced impacts on land and water in discontinuous permafrost: A review of the  
1043 Taiga Plains and Taiga Shield, northwestern Canada, *Earth-Science Reviews*, 232, 104104, ISSN  
1044 0012-8252, <https://doi.org/10.1016/j.earscirev.2022.104104>, 2022.  
1045

1046 Zellweger, F., Coomes, D., Lenoir, J., *et al.*: Seasonal drivers of understorey temperature buffering  
1047 in temperate deciduous forests across Europe, *Global Ecol. Biogeogr.*, 28, 1774–1786, <https://doi.org/10.1111/geb.12991>, 2019.  
1048  
1049

1050 Zellweger, F., *et al.*: Forest microclimate dynamics drive plant responses to warming, *Science*, 368,  
1051 772–775, <https://doi.org/10.1126/science.aba6880>, 2020.